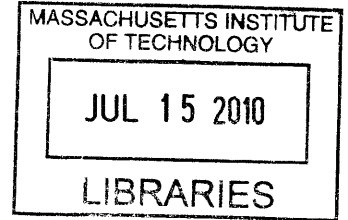# Numerical Simulation of Mixing in Viscous-Fingering Displacements

by

Birendra Jha

Submitted to the Department of Civil and Environmental Engineering
in partial fulfillment of the requirements for the degree of

Master of Science in Civil and Environmental Engineering

at the

MASSACHUSETTS INSTITUTE OF TECHNOLOGY

June 2010

Author . . . .
Department of Civil and Environmental Engineering
May 21, 2010

Certified by . . . .
Ruben Juanes
Assistant Professor of Civil and Environmental Engineering
Thesis Supervisor

Certified by . . . . .
Luis Cueto-Felgueroso
Postdoctoral Associate of Civil and Environmental Engineering
Thesis Supervisor

Accepted by . . . .
Daniele Veneziano
Chairman, Departmental Committee for Graduate Students

Numerical Simulation of Mixing in Viscous-Fingering Displacements

by

Birendra Jha

Abstract

Mixing of two fluids in viscously unstable displacements is far from being fully understood. It is not known how mixing efficiency depends on the viscosity contrast between the fluids, especially for adevction-dominated flows (Peclet number $Pe > 10^3$). It is well known that when a less viscous fluid displaces a more viscous fluid, the displacement front is unstable and leads to the formation of a pattern known as viscous fingering. However, current simulation technology is unable to cope with large viscosity contrasts ($M > 30$). We develop a high-resolution simulation approach that is stable for arbitrary viscosity ratios, and we study mixing under different canonical configurations with viscosity contrasts up to $M = 400$. We explain the observed evolution in degree of mixing through numerical simulation and dimensional analysis. We compute degree of mixing from decay in concentration variance and relate it to the stretching of material interface between the fluids due to fingering. Our analysis predicts the optimum range of viscosity contrast and Peclet number that maximize fluid-fluid interfacial area by balancing the number of fingers with their length before diffusive mixing across the sharp interface takes over. Interesting fingering patterns such as channeling and tip-splitting play an important role in this balancing act which makes degee of mixing a non-monotonic function of viscosity contrast and Peclet number.

Thesis Supervisor: Ruben Juanes
Title: Assistant Professor of Civil and Environmental Engineering

Thesis Supervisor: Luis Cueto-Felgueroso
Title: Postdoctoral Associate of Civil and Environmental Engineering

Acknowledgments

I am grateful to my research advisors, Prof. Ruben Juanes, and Dr. Luis Cueto-Felgueroso for their valuable guidance during this project. I am grateful to my friends & fellow graduate students at Parsons Lab, among them Christopher MacMinn, Michael Szulczewski, Peter Kang, and many others, for their valuable questions and suggestions at various occasions. I am very grateful to my beloved wife, Ashwini Rao, for her encouragement and support. I am here at MIT because of her confidence in my abilities. I am grateful to my mother, Uttama Devi, and my elder brother, Arbind Jha, for their support and love.

Lastly, I acknowledge the contributions of many great researchers who worked in this field and are no more. I try to learn from them.

Contents

List of Figures

9

11

Chapter 1

Introduction

1.1 Mixing of two fluids

Mixing results in a reduction of nonuniformities or gradients in composition and other properties of the mixture by increasing the randomness of its spatial distribution. Molecular diffusion is the mechanism ultimately responsible for creating microscopic homogeneity in fluids where the particles to be mixed are the molecules of the two fluids. However, the mixing process can be sped up by introducing turbulence or laminar chaotic flow condition by mechanical agitation or stirring of the mixture. The latter is the method of choice for low Reynolds number flows ranging from large-scale geophysical flows to small-scale micromixers and microscale biological flows. Under this enhanced mixing concept, the relevant questions are: how fast can a desired state of mixing be achieved; and how does the rate of mixing depend on diffusivity and stirring protocol? These problems have been looked at in the past for fluids of similar viscosities under various mixing conditions and there is some understanding of how the mixing time depends on the diffusivity and flow field of the mixture [27, 28, 29]. For example, various studies predict an exponential decrease in mixing time under chaotic advection conditions [17, 40, 12], that is, conditions leading to complex Lagrangian trajectories of the fluid particles where neighboring fluid particles diverge exponentially with time, rapidly visiting different regions of the fluid which is required for efficient mixing. Such chaotic velocity fields lead to length

13

scales in concentrations (or any other scalar) much smaller than the minimum length scale of the velocity field.

Mixing in viscous-fingering displacements is similar to chaotic mixing as far as unsteadiness of the velocity field is concerned which becomes the primary agent for enhanced mixing because it stretches and shears material surfaces. However, in viscous fingering the velocity field is strongly coupled to the concentration field. Velocity field has sharp gradients at the interfaces and mixing also results in a decay of velocity fluctuations and overall energy of the system which brings viscous fingering closer to turbulent mixing of a scalar, another heavily researched field [10, 50, 30, 36]. Chaotic advection may, in fact, be considered a limiting case of a special type of turbulence known as Batchelor-regime turbulence, e.g. in a purely straining flow, except that the time dependence is deterministic instead of being random. An outcome of velocity-concentration nonlocal coupling, exclusive to viscous fingering displacements, is channeling where less viscous fluid 'shoots' through more viscous medium without actively mixing (Fig. 1-1). At high R, chaneling can induce shielding and branching in adjacent fingers which can potentially pinch-off the main channel if they are close enough and have enough supply of less viscous fluid. Also, there is no mechanical folding of the interface in unidirectional flow with monotonic concentration-viscosity profile. As a result of all these, mixing in viscous fingering displacements does not quite reach the efficiency of choatic mixing.

1.2 Motivation for current work

The viscous fingering phenomena in miscible displacements has been studied in the past, both through lab experiments and numerical simulations, to explain the onset and growth of instabilities as a function of the viscosity contrast and Peclet number (e.g. see reviews in [16], [55] and [56]). A number of experimental, theoretical and numerical works have recently been devoted to the understanding of various aspects of the instability [31, 58, 1, 22, 19, 8, 34]. Linear stability analysis for the growth of instabilities under various conditions (anisotropy, heterogeneity, gravity, capillarity,
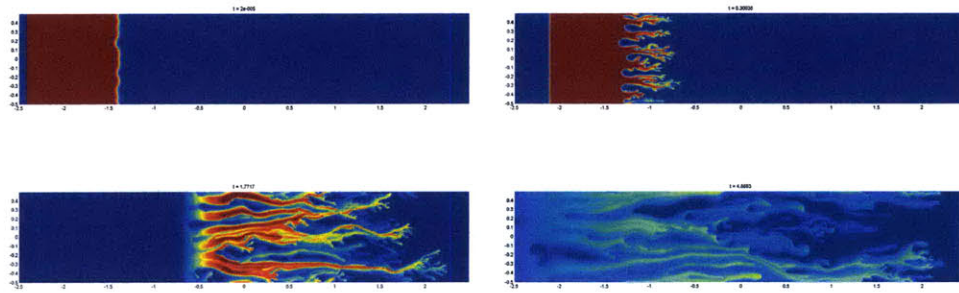
Figure 1-1: Concentration fields at different times from a single-slug simulation in a periodic domain for $[R, Pe] = [3, 8000]$. Red color denotes less viscous fluid with concentration $c = 1$ and blue color denotes more viscous fluid with concentration $c = 0$. As the slug is displaced to the right, it develops fingers at the front which show preferential growth along longitudinal direction and vigorous tip-splitting. As the fingers keep growing, mixing of the two fluids across the interface continues to smear out the sharpness of these interfaces. Also, this growth in volume occupied by the less viscous fluid results in a decrease of average concentration inside the slug. Eventually, as a result of this stretching, splitting and dilution, the less viscous fluid is mixed with the more viscous fluid and concentration everywhere becomes equal to the mean concentration, i.e., homogenization is achieved. Mean concentration of the domain remains constant in a periodic simulation.
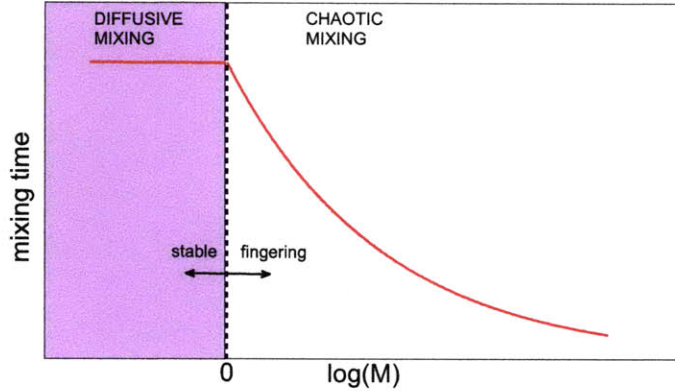
Figure 1-2: Hypothesis of a rapid and monotonic decrease in mixing time with increase in the viscosity ratio.

chemical reaction, radial displacements etc.) have also been performed [32, 41, 43, 57, 54, 52, 53, 37, 35, 14]. Evolution of mixing length, interfacial area between the fluids, width of the fingers and displacement efficiency have been measured and related to the mobility ratio, M, and the Peclet number, Pe, in lab experiments and simulations. Despite the considerable work done, it is yet not known how does the degree of mixing evolve under viscous fingering and what are the optimum mixing conditions in terms of the viscosity contrast and the flow rate. These are important questions to answer, for example, in a micromixer setting [42, 24] where the small dimensions of the mixer requires fast mixing under laminar flow conditions. It is especially difficult for fluids with very small molecular diffusivity. For viscosity-matched fluids, scientists and engineers have been successful in achieving efficient mixing through chaotic advection created by ingenious design patterns and velocity fields. For fluids of different viscosities, it is still an open problem and this is the goal of this study.

We start with the hypothesis that as we increase the viscosity ratio of the fluids in unfavorable direction (less viscous fluid displacing more viscous fluid), we should see faster mixing. Moreover, we also hypothesize that for high enough viscosity contrast, mixing in viscous fingering displacements should tend towards chaotic mixing conditions and we should see exponential decrease in mixing time as a function of logarithm of mobility ratio (Fig. 1-2).

1.3 Governing equations of fluid flow and transport

We consider single phase Darcy flow of two perfectly miscible fluids in a two-dimensional rectilinear porous medium of constant porosity and permeability as our physical model. We rescale space and time such that porosity and permeability are set to be unity in the formulation below. The domain is filled with a more viscous fluid which is then displaced by either a slug of less viscous fluid (slab setup), multiple slugs of less viscous fluid (alternating-injection setup) or by blobs of less viscous fluid (blobs setup). In the blobs setup, which we used to derive analytical results, there are about sixteen blobs randomly placed in five columns inside a square periodic domain filled with more viscous fluid. First and fifth columns, at left and right edge respectively, are split from one column of blobs. Hence, we only have four full columns with about four blobs in each column. This setup is useful to study the decay process during mixing. However, it offers a limited longitudinal length (typical diameter of a blob) for fingering to take place. This limitation results in limited growth of tip-splitting and channeling features during viscous fingering which are pronounced in a slug simulation inside a longer domain (slab setup and alternating-injection setup).

The physical domain is similar to a Hele-Shaw cell by analogy of the flow. Flow is from left to right under a mean velocity field $U = (U, 0)$. The length and width of the domain are L and W, respectively. The viscosity of the less viscous fluid is μ_1 and that of the more viscous fluid is μ_2. The fluids are assumed to be perfectly miscible, neutrally buoyant and incompressible. The diffusivity D between the two fluids is assumed to be constant, isotropic and independent of concentration. We do not distinguish between longitudinal and transverse diffusivity although it is known that they are different because of the velocity field [3, 37]. There have been attempts to capture anisotropic dispersion via Taylor dispersion model [45, 57, 58]. However, validity of this model is limited to Poiseuille type flows of constant viscosity and it has been shown to be ineffective for $R > 1$ [33]. We also see that there is a marked suppression of Taylor dispersion in viscous fingering displacements in lab experiments

of fluid displacement in a Hele-Shaw cell (not shown here).

Characteristic scales used to non-dimensionalize the system are: W for length, $\frac{W}{U}$ for time, U for velocity, μ_1 for viscosity and $\mu_1 UW$ for pressure. The governing mass transport equation in the dimensionless form is,

$$\frac{\partial c}{\partial t} + \nabla \cdot \left(\boldsymbol{u}c - \frac{1}{Pe}\nabla c \right) = 0 \tag{1.1}$$

where c is the dimensionless concentration of the mixture which is 0 for the fluid with higher viscosity and 1 for the fluid with lower viscosity. The Peclet number is defined as $Pe = \frac{UW}{D}$. The viscosity ratio of the fluids is defined as $M = \frac{\mu_2}{\mu_1}$. The concentration field is advected by the velocity field $\boldsymbol{u} = (u_x, u_y)$ which in a porous medium is obtained from Darcy's equation,

$$\boldsymbol{u} = -\kappa(c)\nabla p. \tag{1.2}$$

where p is the pressure field and $\kappa(c)$ is the the concentration-dependent mobility field. Eq. (1.1) is also known as the advection-diffusion equation or ADE. For an incompressible system, conservation of mass for the mixture reduces to the constraint,

$$\nabla \cdot \boldsymbol{u} = 0. \tag{1.3}$$

The mobility is assumed to depend on the concentration of the mixture as,

$$\kappa(c) = \frac{1}{\mu(c)} = e^{-R(1-c)} \tag{1.4}$$

where $R = \log M$. Above, we assume an exponential viscosity-concentration model, i.e., the mixture viscosity decreases exponentially with concentration. For a mobility ratio of $R = 2$, Fig. 1-3 plots dimensionless viscosity as a function of concentration. Exponential viscosity-concentration model has been found to be a reasonable approximation for water-glycol mixtures [34].
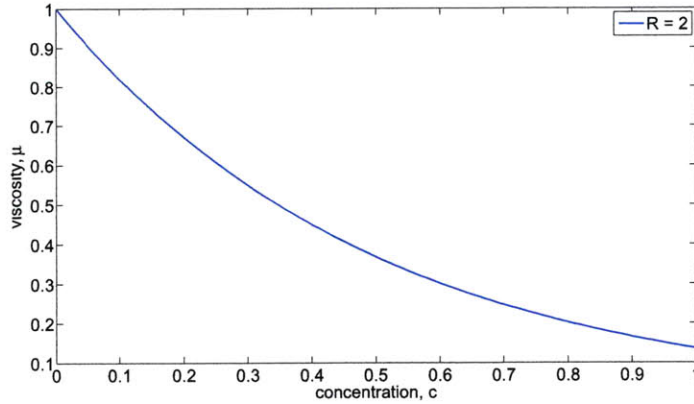
Figure 1-3: Exponential model for mixture viscosity dependence on concentration.

1.4 Boundary and initial conditions

We perform simulations in both a periodic domain and an alternating-injection domain. We use two kinds of boundary conditions: periodic in $x - y$ and alternating-injection in x with periodic in y. Periodic simulations (stripes, blobs, and slab setups) use periodic boundary conditions in x and y directions for both transport and pressure equations. Initial velocity field is uniform in space and comes from the mean flow which is $\boldsymbol{U} = (1, 0)$, after non-dimensionalizing. Initial concentration field varies with the setup. For single-slug simulations or slab setup, a slug of less viscous fluid is placed near the left boundary with perturbations at the front with unfavorable viscosity ratio (right front). Remainder of the domain is filled with the more viscous fluid. The right and left boundaries of the domain have same initial concentration ($c = 0$) as required by the periodic boundary conditions used in this setup. For alternating-injection simulation, the initial concentration field is similar except that the initial slug size is smaller and the slug starts at the inlet boundary. Hence, the inlet and outlet boundaries are at different initial concentrations which is alright considering that we do not use periodicity in x direction for this setup. The perturbations at the unfavorable displacement front are created from a few unstable growth modes of random amplitude and phase. This ensures asymmetric initial conditions which gives better resemblance to viscous fingering experiments carried out in a lab.

19
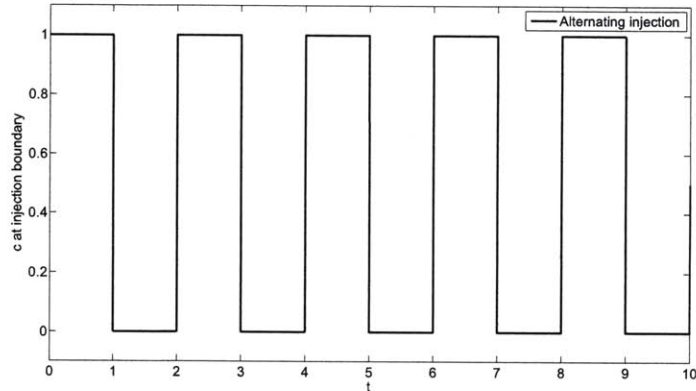
Figure 1-4: Time series of the concentration at the left boundary for the case of alternating injection.
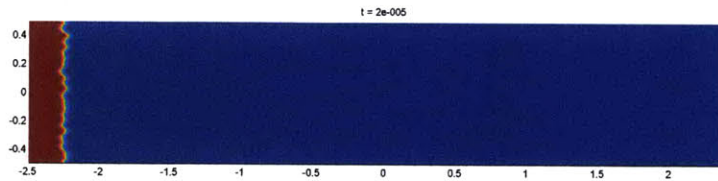
Figure 1-5: Initial concentration field in an alternating-injection simulation.

Alternating-injection simulations have the left boundary condition of alternating injection: low viscosity slug is injected for a unit time duration followed by a high viscosity slug of the same duration (Fig. 1-4). Each low viscosity slug enters with a randomly perturbed front. Outlet boundary is natural flow. For the pressure equation, we use a constant flux boundary at the left inlet and natural flow at the right outlet. Fig. 1-5 shows the initial concentration field for a typical alternating-injection simulation.

1.5   Numerical scheme

Traditionally, Eq. (1.1) and Eq. (1.5) are solved sequentially using spectral methods under periodic boundary conditions which results in a fast numerical solution of the system [44]. Under this scheme, the pressure equation (Eq. (1.3)) is replaced by,

$$\Delta \Psi = -\omega, \qquad (1.5)$$

20

where the streamfunction Ψ is by definition,

$$u_x = \frac{\partial \Psi}{\partial y}, \qquad\qquad u_y = -\frac{\partial \Psi}{\partial x}, \qquad (1.6)$$

and the vorticity (magnitude of the vorticity vector normal to the plane of flow) is related to the gradients in concentration as,

$$\omega = \nabla \times \boldsymbol{u} = R\left(\frac{\partial c}{\partial x}u_y - \frac{\partial c}{\partial y}u_x\right), \qquad (1.7)$$

At a given time step, Eq. (1.7) is used to compute the vorticity field from known concentration and velocity fields. Then Eq. (1.5) is solved in Fourier space under periodic boundary conditions to obtain the streamfunction of the flow. In Fourier space, it is an algebraic equation. Then the velocity field is constructed from streamfunction using Eq. (1.6). Eq. (1.1) is explicitly integrated in time to obtain the concentration field at new time step from the velocity field at the previous step. There is a time step limitation because of the explicit time integration.

This approach is numerically unstable for large values of M (around $M > 30$) when the finger velocity is very high compared to the rest of the flow and therefore it cannot be split as in Eq. (1.5). One can see that in this explicit numerical scheme, Eq. (1.5), tries to obtain the streamfunction of new velocity field from a vorticity computed with old velocity field using Eq. (1.7). This splitting works only if the velocities everywhere in the domain are not too large which is not the case at high M, especially near the tip of the fingers. Therefore, the problem cannot be solved accurately with this traditional numerical scheme. One obvious choice is to solve Eqs. (1.2)-(1.3) directly for the pressure field. This is, of course, computationally more expensive because we need to solve a matrix-vector system instead of one single algebraic equation in Fourier space for Eq. (1.5). On the other hand, we find that this scheme is stable for very high values of M. For alternating-injection simulations where the boundary conditions are not periodic along the flow direction and hence Eq. (1.5) also requires a matrix solve, this scheme performs very well.

In summary, we sequentially solve the system of two PDEs, Eq. (1.1) and Eqs. (1.2)-

(1.3), using sixth order compact finite differences in space and explicit third-order Runge-Kutta scheme in time. For periodic simulations at $R < 3$, we use the spectral scheme with a streamfunction-vorticity formulation, because it is stable and has a lower computational cost.

1.6 Degree of mixing

There are various means of quantifying mixing [39, 48, 25]. We choose the variance of the concentration to define the degree of mixing, χ, as,

$$\chi = 1 - \frac{\sigma^2}{\sigma_{\max}^2} \tag{1.8}$$

where σ^2 is the concentration variance of the mixture, either at a section or inside the whole domain, with respect to a mean concentration of 0.5 and $\sigma_{\max}^2 = 0.25$ is the maximum variance corresponding to a perfectly segregated mixture. We also define a scale of segregation [25] as,

$$L_s = \int_0^W f(r)dr \tag{1.9}$$

where W is the width of the domain and $f(r)$ is the correlation function defined as,

$$f(r) = \frac{1}{\sigma^2} \int_0^W (c(y) - 0.5)(c(y + r) - 0.5)dy \tag{1.10}$$

where concentrations are taken at a fixed x. Both L_s and $f(r)$ can vary in time. In a perfectly mixed state, $\chi = 1$ and $L_s = 0$. We can similarly define a time scale of segregation at a given point and analyze homogeneity in mixing after certain time.

1.7 Previous work

Previous work in this area has focused on turbulent mixing of a passive scalar in either a decaying or sustained turbulent velocity field [10, 50, 30, 36] and on chaotic advection driven mixing using time-periodic velocity fields e.g. Sine Flows of different

periods [49, 7, 20]. More recently, successful application of an eddy diffusivity model, derived within the general framework of Prandtl mixing theory, to explain turbulent mixing due to Rayleigh-Taylor convective instabilities have been reported [4, 5]. In both cases, turbulent and laminar chaotic mixing, viscosity has been assumed to be constant and there is an assumption of scale separation between the velocity field (which varies on the large scale) and the scalar field (which varies on much smaller scales because of large Schmidt number, i.e., $Sc = \frac{\nu}{D} \gg 1$, especially in liquids). This allows the scalar within each fluid element to evolve, independently of all other elements. In this description the scalar variance decays within each fluid element at a rate depending on the time history of the local flow. Taking the ensemble average over all such histories gives the decay rate of the total scalar variance. Here the focus has been on the study of the decay of concentration variance under various initial and boundary conditions (e.g. effect of initial length scale ratio between velocity and scalar fields and effect of no-slip conditions on walls), effect of different flow geometries and different velocity fields. Recently, a more global approach to understand the scalar decay has been proposed that suggests computing this rate from the effect of flow on the gravest spatial Fourier modes of the system [12]. However, studies like these consider the action of advection and diffusion in succesive steps, instead of being simultaneous, based on the argument that when advection is active, diffusion can be ignored if the diffusivity is very low.

The goal of this study is to explain the evolution of mixing under the action of viscous fingering. We use alternating-injection scenario as the main set-up but also look at purely decaying scenario where a single slug of less viscous fluid displaces more viscous fluid or a number of blobs of more viscous fluid flow through a domain filled with the less viscous fluid. We use numerical simulations and dimensional arguments as our tools. We also study the statistics of the concentration field and structure of the viscous fingers to characterize the anisotropy and inhomogeneity in mixing. We relate the degree of mixing and its inhomogeneity to dimensionless governing parameters of the displacement process, namely, viscosity ratio and Peclet number.

In Chapter 2, we present analytical results based on dimensional analysis and

23

derive a two-equation model for mixing under viscous gingering. In Chapter 3, we describe simulation results of viscous fingering in spatially periodic domain. In Chapter 4, we describe simulation results with alternating-injection boundary condition. In Chapter 5, we highlight the anisotropy and inhomogeneity of mixing inside the domain. In Chapter 6, we summarize the results and give concluding remarks.

Chapter 2

Analytical results

There are two issues in Eq. (1.1) that influence the numerical solution scheme and the behaviour of the solution. While Eq. (1.1) is a second-order linear parabolic PDE in c, the relation between $c(\boldsymbol{x}, t)$ and $\boldsymbol{u}(\boldsymbol{x}, t)$ makes it nonlinear. Nonlinearity in Eq. (1.1) shows up in the advective flux term $\boldsymbol{u}c$. More importantly, the nonlinear relation between $\boldsymbol{u}$ and ensemble averaged concentration, $\langle c \rangle$, makes it very difficult to predict properties of average concentration distribution, such as its mean and variance, over different initial conditions and perturbations in velocity field. This is the kind of nonlinearity that has given rise to 'moment closure problem' in turbulence. In turbulence, it is the fluctuations in the velocity field that is difficult to relate to the mean concentration field; in viscous fingering, it is the mobility equation, Eq. (1.4), that makes it nonlinear and difficult to relate the two.

The other issue with Eq. (1.1) is that the assumption of separation of scales between concentration and velocity fields breaks down because of the presence of coherent structures (fingers). The fluctuations in velocity field are of the same length scale as the scale of the fingers. In high Pe displacements, the velocity field has a large range of spatio-temporal scales all the way up to the observational scale of the domain. If the fluctuations in the velocity field were at a much smaller scale with short-range correlations than those in the concentration field, as is assumed in mixing-length theory [46] and homogenization theory [23, 18, 21], then it would have been possible to define an Eulerian effective dispersivity in Eq. (1.1) that lumps advective

flux with dispersive flux. Because of this, in the present case other means of defining an effective diffusivity is sought by Lagrangian-mean methods [26].

In the first section we compare results from linear stability analysis (LSA) of viscous fingering process [43] to that from our nonlinear numerical simulations. This verifies that our simulations accurately predict onset of instabilities at early time when LSA is valid. During the nonlinear regime that follows, we do not have any analytical results from the literature for the growth of finger width. This growth in transverse direction eventually leads to mixing and, therefore, it is important to understand its evolution as a function of the mobility ratio and the Peclet number. In the next section, we perform a dimensional analysis for length scale of fingers and capture its evolution in time as a power law function in this nonlinear diffusive regime. A central result is that the length scale of fingers first decreases with time, when the fingering process dominates diffusion, because instabilities at the front grow along x and thins along y. This leads to a characteristic dip or sag in the time evolution of this length scale. The magnitude and timing of this dip is directly related to the strength of fingering and ultimately to the degree of mixing. As we will see, this length scale is proportional to the ratio of concentration variance and mean dissipation rate. In the third section of this chapter we derive evolution equations for these two quantities. This two-equation model elucidates the relation between degree of mixing and the governing parameters of the process, i.e., the mobility ratio and the Peclet number.

2.1 Comparison with linear stability analysis

We know that under quasi-steady-state approximation (QSSA) of the base state [43], the linear stability analysis (LSA) can predict growth rate for each wavenumber in the initial perturbation of the interface between the two fluids. Tan and Homsy [43] reported this for exponential viscosity-concentration relationship and, before them, Chuoke (in the appendix of [13]) did this for linear viscosity-concentration relationship. QSSA predictions are approximate because of a diffusive base state that changes in time. They overestimate the growth rates at very early times because they do not
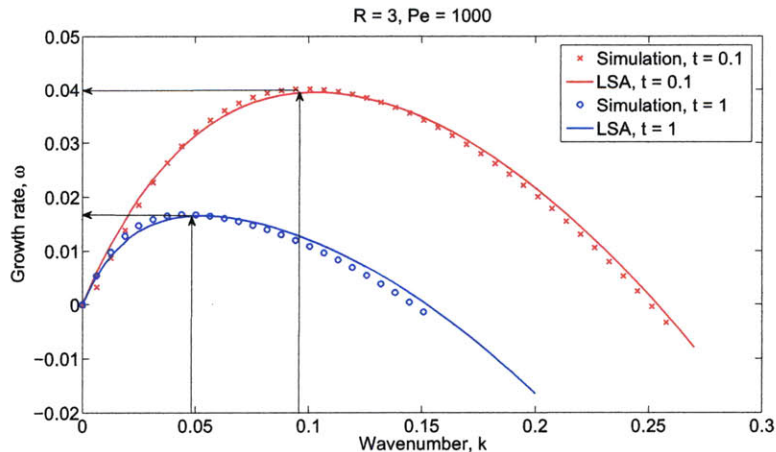
Figure 2-1: Dispersion relation for $R = 3, Pe = 1000$. Arrows indicate most dangerous modes at successive time steps.

take into account dampening of the instabilities due to axial dispersion. Nonetheless, such predictions have been found to be in good agreement with experiments and numerical simulations of viscous fingering displacements in linear regime. We follow this method to obtain a growth rate for each wavenumber by solving an eigenvalue problem derived from the perturbation to the base state. At the same time, we obtain growth rate for the same wavenumbers from our numerical simulation by assuming perturbations of normal mode shapes. The resulting dispersion relation between growth rate and the wavenumber of the perturbation is shown in Fig. 2-1 and the agreement between LSA and the simulations is good.

In a homogeneous isotropic system, the growth rate and wavenumber of the most dangerous mode at $t = 0$ can be derived analytically [43]. They scale with R and Pe as follows,

$$\omega_m = 0.0225 R^2 Pe, \quad k_m = 0.118 R Pe \tag{2.1}$$

where subscript m refers to the most dangerous mode.

LSA gives information about the finger width and its growth at the onset of instability. As R increases, this width goes down. Under the assumption of normal modes in instabilities, the amplitude of the perturbation or finger length grows exponentially in time with a growth rate proportional to R^2. In the nonlinear regime,

due to the coupling with the pressure field, this is responsible for channeling of the less viscous fluid slug-after-slug. Increasing Pe leads to a decrease in finger width. In the nonlinear regime, it leads to an elongation of fingers if Pe is below a certain threshold value beyond which tip splitting ensues. In both cases, higher Pe leads to an increase in interface length between the fluids. However, as we will see later, there is an optimum Pe that results in the largest interface length at a given R. The dependence of finger length and width on Pe is observed to be weaker than on R and it saturates for high enough Pe at late times.

It is essential to know how the fingering structure evolves in the nonlinear regime if we want to understand the evolution of mixing. In the nonlinear regime, merging, shielding, splitting (tip and side), channeling, fading are different mechanisms of interactions among fingers as already identified in numerical simulations and lab experiments. The typical width of the finger changes through these mechanisms. Therefore, it is important to understand the dependence of finger width on the governing parameters. Dimensional analysis provides one such tool that can be used to investigate self-similarity of finger width in R and Pe.

2.2 Dimensional analysis of finger width

Let w' be the typical width of a viscous finger. The input parameters to the system are fluid viscosities μ_1 and μ_2, diffusivity D between the fluids, mean velocity U and dimensions of the domain L and W. Since we observe that finger width evolves in time, let time t' also be an independent input parameter in determining w'. We consider time large enough so that effect of initial conditions vanish. Therefore, we can write,

$$w' = w'(\mu_1, \mu_2, U, D, L, W, t').$$ (2.2)

where all the quantities are dimensional. Now, for a large enough domain, that is, large enough L and W, the finger width should not be a function of L and W. In

other words, boundary effects vanish and we can write,

$$w' = w'(\mu_1, \mu_2, U, D, t').$$ (2.3)

The assumption over the range of t' and w' such that details of initial and boundary structure vanish is standard in the field of intermediate asymptotics [2]. This is precisely the regime where underlying laws governing evolution of finger width appear most clearly.

The dimensional analysis argument is as follows [2]. Above, w' is a function of five parameters. Among these five parameters, we identify parameters with independent dimensions and parameters with dependent dimensions, noting that w' is obviously a parameter with dependent dimension. Each parameter with dependent dimension can be substituted by a dimensionless parameter which is the ratio of that parameter and the unique product of powers of the parameters with independent dimensions. This step reformulates the dimensional equation (Eq. (2.3) in our case) as an equation for a dimensionless parameter expressed as a product of powers of parameters with independent dimensions and a new function of dimensionless parameters only. The number of unknown parameters in this new function has decreased by the number of parameters with independent dimensions and that is the main benefit of dimensional analysis.

In Eq. (2.3), we identify w', μ_2 and t' as parameters with dependent dimensions and μ_1, U and D as parameters with independent dimensions. We identify three dimensionless parameters in accord with Π-theorem [6],

$$\Pi = \frac{w'}{D/U} = \frac{w'/W}{D/UW} = wPe, \; \Pi_1 = \frac{\mu_2}{\mu_1} = M, \; \Pi_2 = \frac{U^2 t'}{D} = \frac{UWt}{D} = tPe \quad (2.4)$$

We can see that Π is the product of dimensionless finger width $w = \frac{w'}{W}$ and Pe, Π_1 is the dimensionless viscosity ratio M and Π_2 is a product of dimensionless time $t = \frac{t'}{W/U}$ and Pe. Now, not knowing anything else, we can still write Π as a function of the

original set of parameters modified with the newly identified dimensionless group,

$$\Pi = \Pi(\mu_1, \Pi_1, U, D, \Pi_2) \tag{2.5}$$

because μ_2 can be replaced by $\Pi_1 \mu_1$, and t' can be replaced by $\frac{\Pi_2 D}{U^2}$. In Eq. (2.5), if we change the unit of mass, it changes μ_1 but it does not change U, D, Π_1, Π_2 or Π. So, Π must be independent of μ_1. Next, if we change the unit of length, it changes U and D but it does not change Π_1, Π_2 or Π. Lastly, changing unit of time changes U and D but does not affect the remaining parameters Π_1, Π_2 and Π. Hence, Π must be independent of both U and D as well. Therefore, Eq. (2.5) reduces to,

$$\Pi = \Pi(\Pi_1, \Pi_2) \tag{2.6}$$

Now, restoring Π as dimensionless width we obtain,

$$w = \frac{1}{Pe} \Pi(M, tPe) \tag{2.7}$$

Thus the original problem of determining w' as a function of five variables is now reduced to determining w as a function of two parameters. This satisfies the Π-theorem in dimensional analysis, i.e., number of dimensionless parameters in the function (two) is equal to the total number of governing parameters (five) minus the number of parameters with independent dimensions (three).

One way to test Eq. (2.7) would be to plot the scaled dimensionless finger width, wPe, against scaled dimensionless time, tPe, from simulations with different (but high) Pe and fixed M and check if the points fall on a single curve. If so, this curve provides the form of the function Π, at a fixed M. We will follow this approach to demonstrate the self-similarity of the second kind in dimensionless parameter tPe, which means,

$$wPe = f(M)(tPe)^\alpha \tag{2.8}$$

30

where f is an unknown dimensionless function of M. In principle, α can still depend on M and cannot be determined from dimensional analysis. Eq. (2.8) can be seen as a self-similar asymptotic solution of the original problem in Eq. (2.2) in intermediate range of time (far from the influence of initial and boundary details). Original problem may be non-self-similar due to characteristic length and time scales. To determine $f(M)$, we can follow the same recipe of plotting $\frac{wPe}{(tPe)^\alpha}$ against M and check if we obtain a similarity of the first kind (independent of M) or the second kind (power-law asymptotic behaviour in M). We find that M is not a similarity parameter of either kind.

At early time finger width drops due to fingering. Later, in the diffusion-dominated regime following the fingering regime, finger width increases in a power-law fashion with time. To find the power-law exponent, we plot $wPe - tPe$ for different R and Pe (Fig. 2-2). To find the exponent α, we fit a power-law type equation to the background trend in the data. The similarity relation we observe has the following form,

$$wPe = C(tPe)^\alpha \tag{2.9}$$

where $C = f(M)$ is constant for a fixed R and α is the power-law exponent. The dependence of α on R is investigated by plotting wPe against tPe for different R (Fig. 2-2). We note that during the evolution this exponent is higher initially and then it decreases gradually towards a value of 0.5. This kind of transition in α is because of the blobs setup. Initially when fingering begins, finger width drops. Then it rises due to the merging of the adjacent fingers, both convectively and diffusively. In a blobs setup, we get lots of small fingers within each blob that cannot grow longitudinally because of the limited size of the blobs. So the merging starts quickly leading to a faster rise in finger width (higher α). However, after certain time, channel like features appear out of several merged fingers and they span the length of the domain. There are about four to five of these channels across the width of the domain separated by islands of more viscous fluids. This inhibits the growth of finger width and α starts to decline.
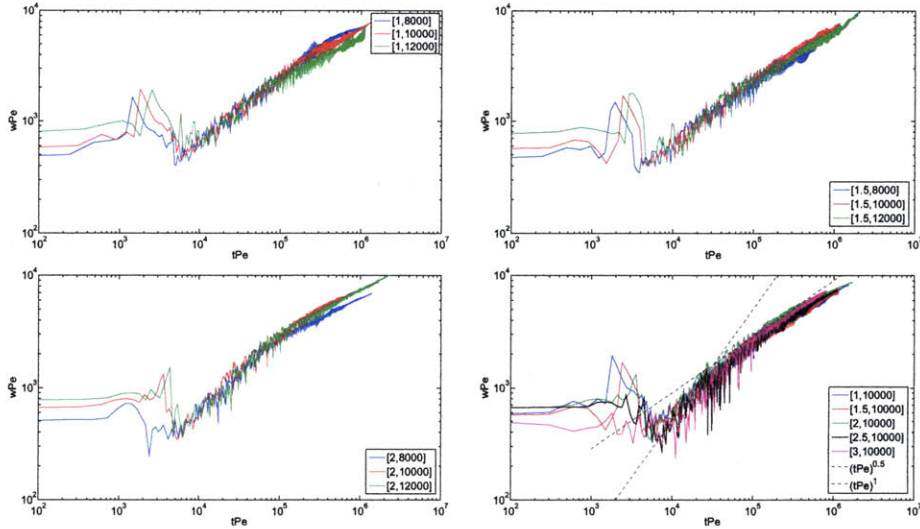
Figure 2-2: Evolution of wPe with tPe for different R and Pe in blobs simulations. Finger width evolves as a power-law in time with exponent independent of Pe. For $R = 1, 1.5, 2, 2.5$, and 3 the exponent at late time is approximately 0.5 and, hence, also independent of R (figure on bottom right). Coefficient C is also approximately constant for the range of R investigated.

In a single-slug simulation (slab setup) also, we get the power-law evolution of finger width but the scaling is different. This is because the fingering continues for a longer duration compared to the blobs setup. During this time, vigorous splitting and merging takes place in the transverse direction leading to a faster rise in the finger width. Therefore, in a longer domain α is higher than in a shorter domain. Fig. 2-4 and Fig. 2-5 show that the exponent α is 1.0 for $R = 3$ in a single-slug simulation. The exponent is again independent of Pe. To confirm that α indeed is smaller in a shorter domain, we conduct slab simulation in a square domain ($L : W = 1 : 1$) as well. As expected, less merging takes place and rise in finger width is slower. Fig. 2-3 shows that α is indeed smaller, 0.5, as also observed in blobs setup at late times.

Thus, α depends on the physical setup e.g. initial concentration field, domain aspect ratio etc. Next, the relation of C with R is also explored to obtain the form of $f(M)$ in Eq. (2.8). We find that for a given setup, C is mostly insensitive to changes in R and Pe (Fig. 2-2). In summary, Eq. (2.8) obtained through dimensional analysis can capture the coarsening of the finger structure in the nonlinear regime.
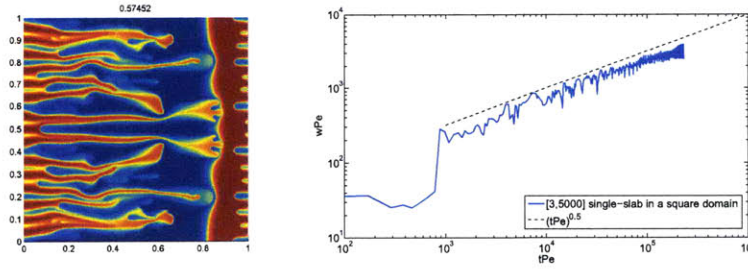
Figure 2-3: Slab simulation inside a square domain. Left figure shows a snapshot of the concentration field. Right figure shows evolution of wPe with tPe at a section in the domain. Power-law exponent is 0.5, different from the slab simulation inside a rectangular domain for same R and Pe. It is also different from the blobs setup at early times. This confirms that α depends on the aspect ratio of the domain as well as the initial concentration field.
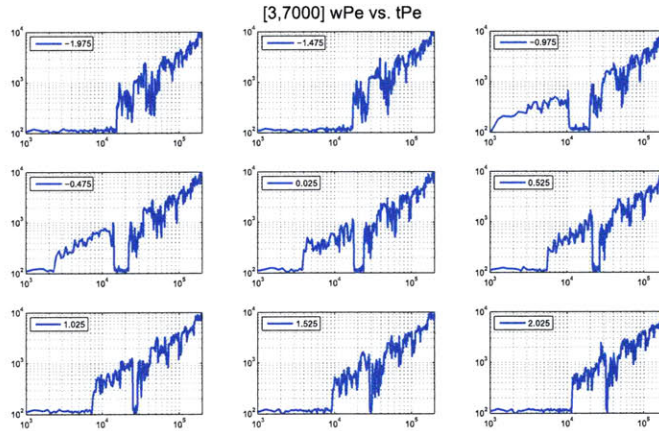
Figure 2-4: Evolution of wPe with tPe at nine different x-sections from a slab simulation.
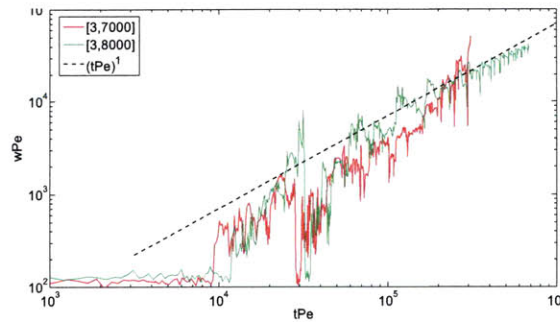
Figure 2-5: Evolution of finger width in slab simulations at two different Pe. Evolution follows a power-law behaviour. Value of the power-law exponent α is independent of Pe.

33

2.2.1 Dissipation length scale as a global measure

We notice that finger width, w, computed at x cross-sections oscillates in time, for example in Fig. 2-2. To avoid these oscillations we can look at a global measure of length scale in the problem such as the scale of dissipation at the interface of two fluids [46, 10], defined in dimensionless quantities as,

$$s = \sqrt{\frac{\sigma^2}{\epsilon Pe}} \tag{2.10}$$

where σ^2 is the variance of concentration field defined as,

$$\sigma^2 \doteq \langle c^2 \rangle - \langle c \rangle^2, \tag{2.11}$$

and ϵ is the volume-averaged dissipation rate (non-dimensionalized) defined as,

$$\epsilon = \frac{1}{Pe} \langle |\boldsymbol{g}|^2 \rangle, \tag{2.12}$$

where $\boldsymbol{g} = \nabla c$. Hence, Eq. (2.10) can be written as,

$$s = \sqrt{\frac{\sigma^2}{\langle |\nabla c|^2 \rangle}} \simeq \frac{\sigma}{\langle |\boldsymbol{g}| \rangle}, \tag{2.13}$$

where we have used $\langle |\boldsymbol{g}|^2 \rangle \sim \langle |\boldsymbol{g}| \rangle^2$ which is verified through simulations.

Just like finger width w, scalar dissipation length s is a transverse length scale in the problem. It can be interpreted as the thickness of the interface on which the concentration gradients are localized. It is also referred to as Taylor microscale for the scalar fluctuations [46]. Scalar dissipation length is equivalent to the viscous length $l \sim \left(\frac{\nu L}{U}\right)^{1/2} = L Re^{-1/2}$ where ν, L, U, and Re are kinematic viscosity, macroscopic length scale, mean velocity and Reynolds number of the flow, respectively. The viscous length l relates to the molecular diffusion of momentum deficit across the flow and scalar dissipation length s relates to the molecular diffusion of concentration gradient across the flow. We note that s and w should evolve similarly in a given

(A) $[R, Pe] = [0,10000]$

(B) $[R, Pe] = [1,10000]$

(C) $[R, Pe] = [1.5,10000]$

(D) $[R, Pe] = [2,10000]$
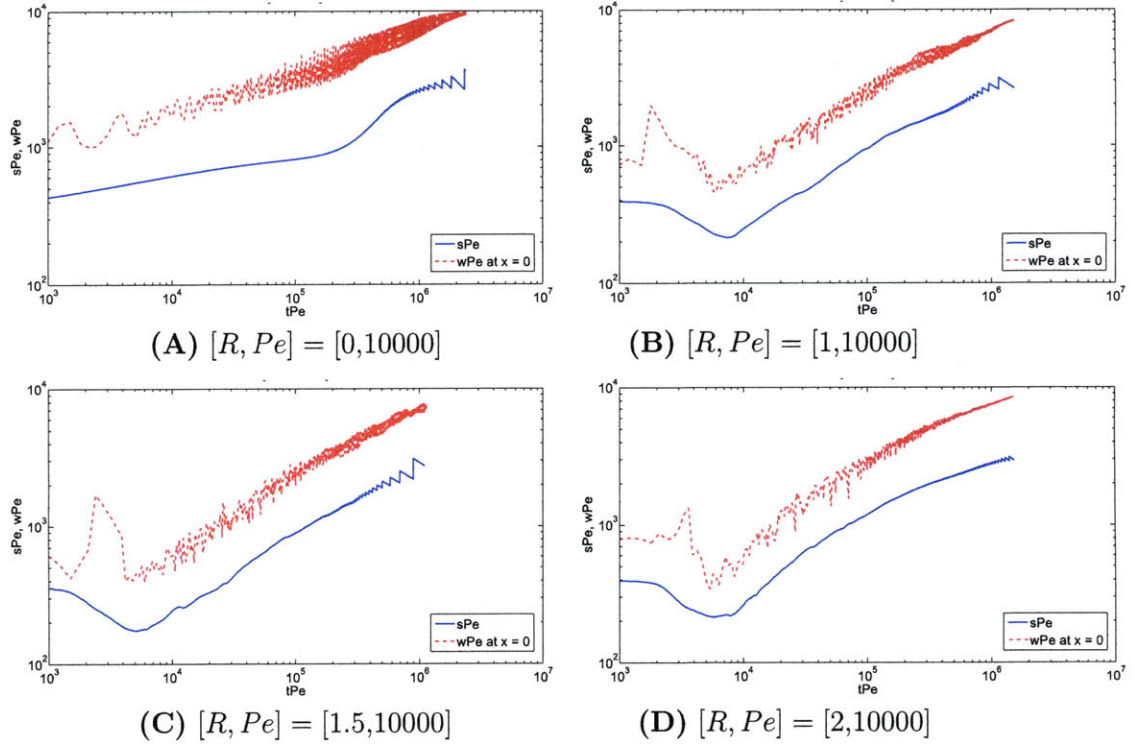
Figure 2-6: Dissipation length scale, s, evolves similar to finger width w.

simulation because they are related to the characteristic length scale of the problem (Fig. 2-6). Under the assumption of equilibrium and self-similarity in viscous fingering process, one length scale can be used to characterize the process because all scales adjust to flow changes at the same rate.

2.3 Two-equation ($\sigma^2 - \epsilon$) model

Mixing is the decay of concentration variance also known as the scalar energy. Best mixing means achieving fastest decay in variance. Decay of variance is given by the dissipation rate. Thus best mixing means achieving highest dissipation rate. Since dissipation rate is directly related to the interfacial length between the fluids, highest dissipation rate results from largest interfacial area. Fingering creates interfacial area through stretching and splitting, as a function of the mobility ratio and the Peclet number. Therefore, highest interfacial length corresponds to the optimum

35

combination of the mobility ratio and the Peclet number for mixing. In this section we will focus on characterizing dissipation rate as a function of the mobility ratio and the Peclet number to achieve best mixing.

We will first obtain an evolution equation for scalar energy $\frac{1}{2}c^2$. Consider flow in a two-dimensional porous domain governed by set of equations Eq. (1.1), Eq. (1.2), Eq. (1.3) and Eq. (1.4). Now, multipling Eq. (1.1) by c gives,

$$c\frac{\partial c}{\partial t} + c\boldsymbol{u} \cdot \nabla c = \frac{1}{Pe}c\nabla^2 c \tag{2.14}$$

We can express this as an equation in c^2. Expanding the right hand side at the same time,

$$\frac{1}{2}\left(\frac{\partial c^2}{\partial t} + \boldsymbol{u} \cdot \nabla c^2\right) = \frac{1}{Pe}\left(\nabla \cdot (c\nabla c) - |\nabla c|^2\right) \tag{2.15}$$

Since $\nabla \cdot (c\nabla c) = \frac{1}{2}\nabla^2 c^2$, we can write,

$$\left(\frac{\partial}{\partial t} + \boldsymbol{u} \cdot \nabla - \frac{1}{Pe}\nabla^2\right)\frac{1}{2}c^2 = -\frac{1}{Pe}|\nabla c|^2. \tag{2.16}$$

which is an evolution equation for $\frac{1}{2}c^2$.

Next, we will obtain an evolution equation for variance of concentration, which characterizes mixing, by averaging Eq. (2.15) over the domain,

$$\frac{1}{2}\left\langle\frac{\partial c^2}{\partial t} + \boldsymbol{u} \cdot \nabla c^2\right\rangle = \frac{1}{Pe}\langle\nabla \cdot (c\nabla c) - |\nabla c|^2\rangle. \tag{2.17}$$

where spatial averaging operator is defined over the volume V of the domain as,

$$\langle \cdot \rangle \equiv \frac{1}{V}\int_V (\cdot)\,\mathrm{d}V. \tag{2.18}$$

Using divergence-free condition, i.e., Eq. (1.3),

$$\boldsymbol{u} \cdot \nabla c^2 = \nabla \cdot (c^2\boldsymbol{u}) \tag{2.19}$$

36

Applying divergence theorem gives,

$$\langle \nabla \cdot (c^2 \boldsymbol{u}) \rangle = \frac{1}{V} \int_S c^2 \boldsymbol{u} \cdot \hat{\boldsymbol{n}} dS \qquad (2.20)$$

and,

$$\langle \nabla \cdot (c \nabla c) \rangle = \frac{1}{V} \int_S c \nabla c \cdot \hat{\boldsymbol{n}} dS \qquad (2.21)$$

where S is the surface bounding V, dS the element of boundary area, and $\hat{\boldsymbol{n}}$ the outward-pointing normal to the boundary. Since we have assumed periodicity in x and y, these two terms vanish and Eq. (2.17) becomes,

$$\frac{\mathrm{d}\langle c^2 \rangle}{\mathrm{d}t} = -\frac{2}{Pe} \langle |\nabla c|^2 \rangle \qquad (2.22)$$

Eq. (2.22) is an evolution equation for variance because the mean concentration $\langle c \rangle$ remains constant in a periodic domain. Hence, the evolution of concentration variance under periodic boundary conditions becomes,

$$\frac{\mathrm{d}\sigma^2}{\mathrm{d}t} = -2\epsilon, \qquad (2.23)$$

which identifies degree of mixing as cumulative dissipation,

$$\chi(t) = 1 - 4\sigma^2(t) = 8 \int_0^t \epsilon dt \qquad (2.24)$$

assuming mixture is perfectly segregated in the beginning with mean concentration of $\langle c \rangle = 0.5$, i.e., $\sigma_0^2 = \sigma_{\max}^2 = 0.25$. Physically, ϵ can be interpreted as a mixing rate, or equivalently as a rate at which scalar fluctuations are destroyed. It can also be understood as a measure of diffusion time scale imposed by the mixing field. Another interpretation of the role of ϵ in Eq. (2.23) is that of a negative diffusion coefficient. Thus, an initially Gaussian distribution, or in our case two-delta distribution, of c would quickly evolve to a delta distribution which corresponds to the homogenization of c towards its mean value.

To obtain the evolution equation for ϵ, we need to extract an equation for $\langle |\boldsymbol{g}|^2 \rangle$

37

from the transport equation. In this way we will also find the dependence of ϵ on the governing parameters R and Pe. We use the analogy in deriving the equation for ϵ_u in the two-equation model of turbulence. There, since $\epsilon_u = \nu \langle |\nabla \times \boldsymbol{u}|^2 \rangle$, to obtain an equation for ϵ_u, one takes the curl of the Navier-Stokes equation, multiplies by $\nabla \times \boldsymbol{u}$ and then applies spatial averaging filter. Here, for the scalar, since $\epsilon = \frac{1}{Pe} \langle |\nabla c|^2 \rangle$, we start by taking the gradient of Eq. (1.1), performing a dot product with $\boldsymbol{g}$ and averaging over the domain. Taking the gradient of Eq. (1.1),

$$\frac{\partial \nabla c}{\partial t} + \nabla \left(\boldsymbol{u} \cdot \nabla c \right) = \frac{1}{Pe} \nabla \left(\nabla^2 c \right), \tag{2.25}$$

and the dot product with ∇c,

$$\frac{1}{2} \frac{\partial |\nabla c|^2}{\partial t} + \frac{\partial c}{\partial x} \frac{\partial}{\partial x} \left(u_x \frac{\partial c}{\partial x} + u_y \frac{\partial c}{\partial y} \right) + \frac{\partial c}{\partial y} \frac{\partial}{\partial y} \left(u_x \frac{\partial c}{\partial x} + u_y \frac{\partial c}{\partial y} \right) = \frac{1}{Pe} \nabla c \cdot \nabla \left(\nabla^2 c \right). \tag{2.26}$$

Expanding,

$$\frac{1}{2} \frac{\partial |\nabla c|^2}{\partial t} + \frac{\partial u_x}{\partial x} \left(\frac{\partial c}{\partial x} \right)^2 + \frac{\partial u_y}{\partial x} \frac{\partial c}{\partial y} \frac{\partial c}{\partial x} + \frac{\partial u_x}{\partial y} \frac{\partial c}{\partial x} \frac{\partial c}{\partial y} + \frac{\partial u_y}{\partial y} \left(\frac{\partial c}{\partial y} \right)^2$$
$$+ \left(u_x \frac{\partial c}{\partial x} \frac{\partial^2 c}{\partial x^2} + u_y \frac{\partial c}{\partial x} \frac{\partial^2 c}{\partial x \partial y} \right) + \left(u_x \frac{\partial c}{\partial y} \frac{\partial^2 c}{\partial x \partial y} + u_y \frac{\partial c}{\partial y} \frac{\partial^2 c}{\partial y^2} \right) = \frac{1}{Pe} \nabla c \cdot \nabla \left(\nabla^2 c \right). \tag{2.27}$$

Since $g_x = \frac{\partial c}{\partial x}, g_y = \frac{\partial c}{\partial y}$, and $\nabla \cdot \boldsymbol{u} = 0$, we obtain,

$$\frac{1}{2} \frac{\partial |\nabla c|^2}{\partial t} + \sum_{i,j} \frac{\partial u_i}{\partial x_j} g_i g_j + \frac{1}{2} \left[\nabla \cdot \left(\boldsymbol{u} g_x^2 \right) + \nabla \cdot \left(\boldsymbol{u} g_y^2 \right) \right] = \frac{1}{Pe} \nabla c \cdot \nabla \left(\nabla^2 c \right). \tag{2.28}$$

Integrating over a periodic domain removes divergence terms on the left hand side.

38

Now, expanding the right hand side,

$$\nabla c \cdot \nabla \left(\nabla^2 c\right) = g_x \frac{\partial^2 g_x}{\partial x^2} + g_x \frac{\partial^2 g_y}{\partial x \partial y} + g_y \frac{\partial^2 g_x}{\partial x \partial y} + g_y \frac{\partial^2 g_y}{\partial y^2}$$

$$= g_x \frac{\partial^2 g_x}{\partial x^2} + g_x \frac{\partial^2 g_x}{\partial y^2} + g_y \frac{\partial^2 g_y}{\partial x^2} + g_y \frac{\partial^2 g_y}{\partial y^2}$$

$$= \nabla \cdot (g_x \nabla g_x) - \left(\frac{\partial g_x}{\partial x}\right)^2 - \left(\frac{\partial g_x}{\partial y}\right)^2 \qquad (2.29)$$

$$\nabla \cdot (g_y \nabla g_y) - \left(\frac{\partial g_y}{\partial x}\right)^2 - \left(\frac{\partial g_y}{\partial y}\right)^2.$$

Again, upon volume integration, divergence terms vanish because of periodic boundary conditions. Therefore, after dividing by the volume V of the domain, we are left with,

$$\frac{1}{2}\frac{\mathrm{d}\langle |g|^2 \rangle}{\mathrm{d}t} + \frac{1}{V}\sum_{i,j}\int \frac{\partial u_i}{\partial x_j} g_i g_j \mathrm{d}V = -\frac{1}{V Pe}\int \left(\frac{\partial g_x}{\partial x}\right)^2 + \left(\frac{\partial g_x}{\partial y}\right)^2 + \left(\frac{\partial g_y}{\partial x}\right)^2 + \left(\frac{\partial g_y}{\partial y}\right)^2 \mathrm{d}V$$

$$= -\frac{1}{V Pe}\int \sum_i |\nabla g_i|^2 \, \mathrm{d}V \qquad (2.30)$$

or,

$$\frac{\mathrm{d}\langle |g|^2 \rangle}{\mathrm{d}t} + \frac{2}{V}\sum_{i,j}\int \frac{\partial u_i}{\partial x_j} g_i g_j \mathrm{d}V = -\frac{2}{Pe}\sum_i \langle |\nabla g_i|^2 \rangle \qquad (2.31)$$

where $\langle |\nabla g_i|^2 \rangle$ is the norm of gradient of the ith component of vector g. Using the definition of mean dissipation rate,

$$\frac{\mathrm{d}\epsilon}{\mathrm{d}t} + \frac{2}{PeV}\sum_{i,j}\int \frac{\partial u_i}{\partial x_j} g_i g_j \mathrm{d}V = -\frac{2}{Pe^2}\sum_i \langle |\nabla g_i|^2 \rangle \qquad (2.32)$$

Alternatively, we can write Eq. (2.32) in direct tensorial notation as follows,

$$\frac{\mathrm{d}\epsilon}{\mathrm{d}t} + \frac{2}{Pe}\langle \nabla u : g \otimes g \rangle = -\frac{2}{Pe^2}\langle \nabla g : \nabla g \rangle \qquad (2.33)$$

As derived above, Eq. (2.33) is an exact equation. Here the advection term is the rate of stretching of the square norm of concentration gradient g. For a globally chaotic

flow with steady or time-periodic velocity fields, the advective term in Eq. (2.33) is simply proportional to $\langle |\boldsymbol{g}|^2 \rangle$. For viscous fingering displacements where velocity field is a function of concentration, it is more complicated.

From Eq. (1.2), we have,

$$
\begin{aligned}
\nabla \boldsymbol{u} = \frac{\partial u_i}{\partial x_j} &= -\mu^{-1} \left(R \frac{\partial c}{\partial x_j} \frac{\partial p}{\partial x_i} + \frac{\partial^2 p}{\partial x_i \partial x_j} \right) \\
&= -\mu^{-1} \left[R \nabla c \otimes \nabla p + \nabla \left(\nabla p \right) \right].
\end{aligned}
\tag{2.34}
$$

Separating the velocity gradient tensor into its symmetric and anti-symmetric part,

$$
\nabla \boldsymbol{u} = \nabla^{\mathrm{s}} \boldsymbol{u} + \nabla^{\mathrm{a}} \boldsymbol{u}
\tag{2.35}
$$

where,

$$
\nabla^{\mathrm{s}} \boldsymbol{u} = \frac{1}{2} \left(\nabla \boldsymbol{u} +^t \nabla \boldsymbol{u} \right), \qquad \nabla^{\mathrm{a}} \boldsymbol{u} = \frac{1}{2} \left(\nabla \boldsymbol{u} -^t \nabla \boldsymbol{u} \right).
\tag{2.36}
$$

Hence the rate-of-strain tensor, which is the symmetric part of the velocity gradient tensor, becomes,

$$
\begin{aligned}
\nabla^{\mathrm{s}} \boldsymbol{u} &= \frac{1}{2} \left(\frac{\partial u_i}{\partial x_j} + \frac{\partial u_j}{\partial x_i} \right) \\
&= -\mu^{-1} \left[R \cdot \frac{1}{2} \left(\nabla c \otimes \nabla p + \nabla p \otimes \nabla c \right) + \nabla \left(\nabla p \right) \right]
\end{aligned}
\tag{2.37}
$$

Assuming $|\nabla \left(\nabla p \right)| \ll |\nabla c \otimes \nabla p|$,

$$
\nabla^{\mathrm{s}} \boldsymbol{u} \sim -\mu^{-1} \left[R \cdot \frac{1}{2} \left(\nabla c \otimes \nabla p + \nabla p \otimes \nabla c \right) \right]
\tag{2.38}
$$

Interface length between the fluids can be expressed as $\langle |\boldsymbol{g}| \rangle V$. Then Eq. (2.34), which is part of the advective term in the evolution of ϵ, means that the rate of stretching of the interface is proportional to the length of the interface. This means a rapid growth in the interface length and consequently in ϵ, when this term is dominant. We will see that the advective term dominates the early time behaviour in ϵ, which

40

rises sharply during this time. Afterwards, ϵ starts to decrease under the influence of the diffusive term. Effect of the second derivative of pressure in Eq. (2.34) is not significant and we verify this assumption by comparing the evolution of kinetic energy dissipation rate, ϵ_u with the scalar dissipation rate, ϵ (Fig. 2-7). The volume-averaged kinetic energy dissipation rate is given by [15, 46],

$$
\begin{aligned}
\epsilon_u &= 2\langle \nu \nabla^s \boldsymbol{u} : \nabla^s \boldsymbol{u} \rangle \\
&= \frac{1}{2} \sum_{i,j} \left\langle \nu \left(\frac{\partial u_i}{\partial x_j} + \frac{\partial u_j}{\partial x_i} \right)^2 \right\rangle
\end{aligned}
\tag{2.39}
$$

Kinematic viscosity $\nu = \mu/\rho$ varies over space and is, therefore, inside the averaging operator. Assuming a uniform average kinematic viscosity $\bar{\nu} = \bar{\mu}/\rho$ and substituting for the rate-of-strain tensor from Eq. (2.37) we obtain,

$$
\begin{aligned}
\epsilon_u &\simeq 2\bar{\nu} R^2 \bar{\mu}^{-2} \sum_{i,j} \left\langle \left[\frac{1}{2} \left(\frac{\partial c}{\partial x_i} \frac{\partial p}{\partial x_j} + \frac{\partial c}{\partial x_j} \frac{\partial p}{\partial x_i} \right) \right]^2 \right\rangle \\
&\simeq 2\bar{\nu} R^2 \bar{\mu}^{-2} \left\langle |(\nabla c \otimes \nabla p)^s|^2 \right\rangle,
\end{aligned}
\tag{2.40}
$$

where superscript s denotes symmetric part of the tensor. From simulations we see that changes in pressure gradient is much smaller than changes in concentration gradient. Pressure field is primarily driven by the mean flow which is uniform over the domain. Under this assumption, which we verify through numerical simulations, we can separate gradients in pressure from gradients in concentration and later replace average of the norm square of pressure gradient with norm square of the average pressure gradient. It follows,

$$
\begin{aligned}
\epsilon_u &\sim 2\bar{\nu} R^2 \bar{\mu}^{-2} \left\langle |\nabla c|^2 \right\rangle \left\langle |\nabla p|^2 \right\rangle \\
&\sim 2\bar{\nu} R^2 \bar{\mu}^{-2} \left| \overline{\nabla p} \right|^2 Pe\epsilon \\
&\sim 2\bar{\nu} R^2 U^2 Pe\epsilon
\end{aligned}
\tag{2.41}
$$

where we have used $U^2 \sim \bar{\mu}^{-2} \left| \overline{\nabla p} \right|^2$ which is from Darcy's equation, relating average pressure gradient to the average velocity. We know average velocity U remains
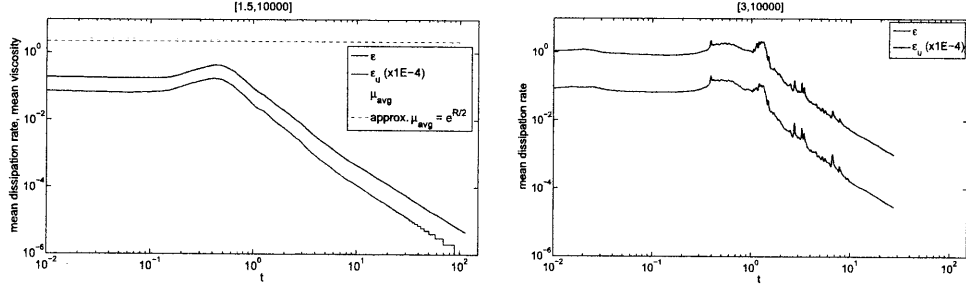
Figure 2-7: On the left, ϵ and ϵ_u are compared from a blobs simulation with $R = 1.5$ and $Pe = 10000$. Notice that $\epsilon_u \sim Pe\epsilon$ as derived in Eq. (2.41). Average mixture viscosity is also plotted in the same plot. On the right, ϵ and ϵ_u are plotted for $R = 3$ and we observe same scaling (note that the second hump between $t = 1$ and $t = 1.5$ is due to numerical errors which are amplified in ϵ and ϵ_u because they are square of the gradients). This validates our assumption that effect of pressure gradient on the temporal scaling of mean dissipation rate is negligible in this periodic setup.

constant in our simulations due to the divergence-free flow. Eq. (2.41) demonstrates that $\epsilon_u \sim \epsilon$ as observed in simulations also (Fig. 2-7).

Now, back to the advective term in Eq. (2.33),

$$
\begin{aligned}
\frac{2}{Pe}\langle \nabla u : g \otimes g \rangle &= \frac{2}{Pe}\langle (\nabla^s u + \nabla^a u) : g \otimes g \rangle \\
&= \frac{2}{Pe}\langle \nabla^s u : g \otimes g \rangle \\
&\sim \frac{2}{Pe}\langle |g \otimes g| \rangle \langle |\nabla^s u| \rangle \\
&\sim -\frac{2}{Pe}\langle |g|^2 \rangle RU\sqrt{Pe} \cdot \epsilon^{1/2}
\end{aligned}
\tag{2.42}
$$

Therefore,

$$
\frac{2}{Pe}\langle \nabla u : g \otimes g \rangle \sim -2RU\sqrt{Pe} \cdot \epsilon^{3/2}
\tag{2.43}
$$

In Eq. (2.42), we assumed symmetry in $g \otimes g$ to replace ∇u by its symmetric part $\nabla^s u$. Similar assumption about symmetry of Reynolds stress tensor is made in derivation of the k equation in the $k - \epsilon_u$ model of turbulence.

Now, for the diffusive term, we have,

$$
\frac{2}{Pe^2}\langle \nabla g : \nabla g \rangle = \frac{2}{Pe^2}\langle |\nabla g|^2 \rangle = \frac{2}{Pe^2}\frac{\langle |\nabla g|^2 \rangle}{\text{var}(g)} \cdot \text{var}(g)
\tag{2.44}
$$

42

Under the assumption of a unique characteristic transverse length scale in the problem (see Subsection 2.2.1), we note that,

$$\frac{\langle g_i^2 \rangle}{\langle |\nabla g_i|^2 \rangle} \sim \frac{\langle c^2 \rangle}{\langle |\nabla c|^2 \rangle}, \qquad\qquad \frac{\langle g_i \rangle}{\langle |\nabla g_i|^2 \rangle} \sim \frac{\langle c \rangle}{\langle |\nabla c|^2 \rangle}. \qquad (2.45)$$

Therefore, we can write,

$$\frac{\text{var}(g_i)}{\langle |\nabla g_i|^2 \rangle} \sim \frac{\text{var}(c)}{\langle |\nabla c|^2 \rangle} \sim s^2 \qquad (2.46)$$

For the diffusive term, this means,

$$\begin{aligned}
\frac{2}{Pe^2} \langle \nabla \boldsymbol{g} : \nabla \boldsymbol{g} \rangle &\sim \frac{2}{Pe^2} \frac{\langle |\nabla c|^2 \rangle}{\text{var}(c)} \cdot \text{var}(\boldsymbol{g}) \\
&\sim \frac{2}{Pe} \cdot \frac{\epsilon}{\sigma^2} \cdot \text{var}(\boldsymbol{g}).
\end{aligned} \qquad (2.47)$$

By definition, $\text{var}(\boldsymbol{g}) = \langle |\boldsymbol{g}|^2 \rangle - \langle |\boldsymbol{g}| \rangle^2$ and $\langle |\boldsymbol{g}|^2 \rangle = \epsilon Pe$. Also, from simulations we find that, $\langle |\boldsymbol{g}|^2 \rangle \sim \langle |\boldsymbol{g}| \rangle^2$. Therefore, we can write,

$$\frac{2}{Pe^2} \langle \nabla \boldsymbol{g} : \nabla \boldsymbol{g} \rangle \sim \text{B} \frac{\epsilon^2}{\sigma^2}. \qquad (2.48)$$

where B is a positive constant. Hence, Eq. (2.33) can be re-written as,

$$\frac{\mathrm{d}\epsilon}{\mathrm{d}t} - \text{A}RU\sqrt{Pe}\epsilon^{3/2} + \text{B}\frac{\epsilon^2}{\sigma^2} = 0, \qquad (2.49)$$

where A and B are positive constants. Eq. (2.49) is a first-order ODE in ϵ. Eq. (2.23) and Eq. (2.49) form a coupled system of two first-order ODEs in time which can be solved with initial values of σ^2 and ϵ. This two-equation model is similar to $k - \epsilon_u$ model in turbulence where k and ϵ_u denote the kinetic energy of the flow and mean energy dissipation rate, respectively (see Appendix A.1). Eq. (2.49) has two power-law terms in $\epsilon - t$ corresponding to fingering-induced enhancement in dissipation rate and diffusion-driven decrease in dissipation rate. The advection term with $\epsilon^{3/2}$ is negative and therefore gives the rising behaviour in ϵ at early times for $R > 0$. The diffusion term with ϵ^2 is positive and therefore gives the declining behaviour in
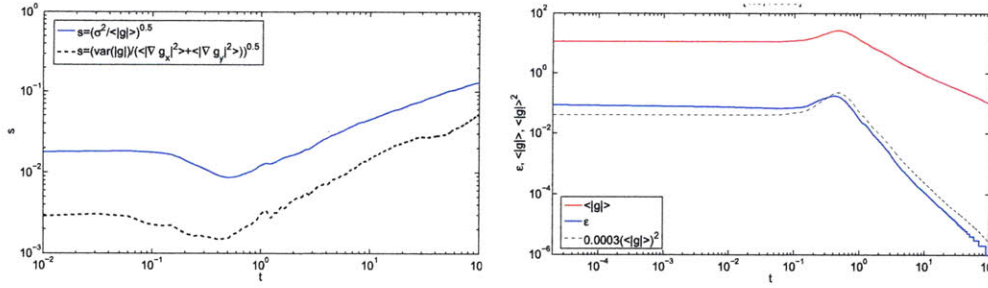
Figure 2-8: Verifying the assumptions made in Eq. (2.48) for the diffusive term. Left figure shows that the length scale computed using $\sqrt{\frac{var(g)}{\langle |\nabla g|^2 \rangle}}$ evolves similar to the dissipation length scale s. Right figure justifies the assumption that average of the norm square of concentration gradient evolves similar to the square of the average of the concentration gradient norm, i.e., $\langle |g|^2 \rangle \sim \langle |g| \rangle^2$. These approximations in s and $\langle |g| \rangle$ allow us to express diffusive term as a function of ϵ and σ^2 in Eq. (2.48)

ϵ at later times. Their combination produces the hump, which is a characteristic signature of fingering, followed by $\epsilon \sim t^{-2}$ scaling at later times. Fig. 2-9 and Fig. 2-11 show the performance of this two-equation model by comparing ϵ and σ^2 from the model with those from the direct simulations. Since σ^2 monotonically decays in time with corresponding approximate scaling of $\sigma^2 \sim t^{-1}$, we can substitute this relation in Eq. (2.49) and solve the single ODE for ϵ. We see that this approximation still captures the hump and the powerlaw decline (Fig. 2-11).

Eq. (2.49) is an approximate equation because of the assumptions made in deriving it. It is derived under assumptions of periodicity, high Pe and a 'closure' hypothesis of one unique length scale (Eq. (2.46)) during the fingering process. The $k - \epsilon_u$ model in turbulence is also valid only at high Reynolds number and away from the boundaries (see Appendix A.1). There is an optimum R and optimum Pe that gives maximum hump in ϵ. At later time, when $\sigma^2 \sim t^{-1}$, it gives the characteristic $\epsilon \sim t^{-2}$ behaviour which translates into $s \sim t^{1/2}$ (Fig. 2-6) which is the diffusion-driven growth of the dissipation length scale in viscous-fingering displacements.

The two-equation model derived in this section has two coefficients A and B which are not universal constants as shown by their values in Fig. 2-9 and Fig. 2-11. In particular, coefficient B is found to be more sensitive to changes in R and Pe. One reason could be the closure hypothesis of a unique length scale invoked to model

Figure 2-9: Mean dissipation rate and variance computed using the two-equation model compares well with the results from numerical simulations. Results are shown for $R = 1, 1.5, 2, 3$.
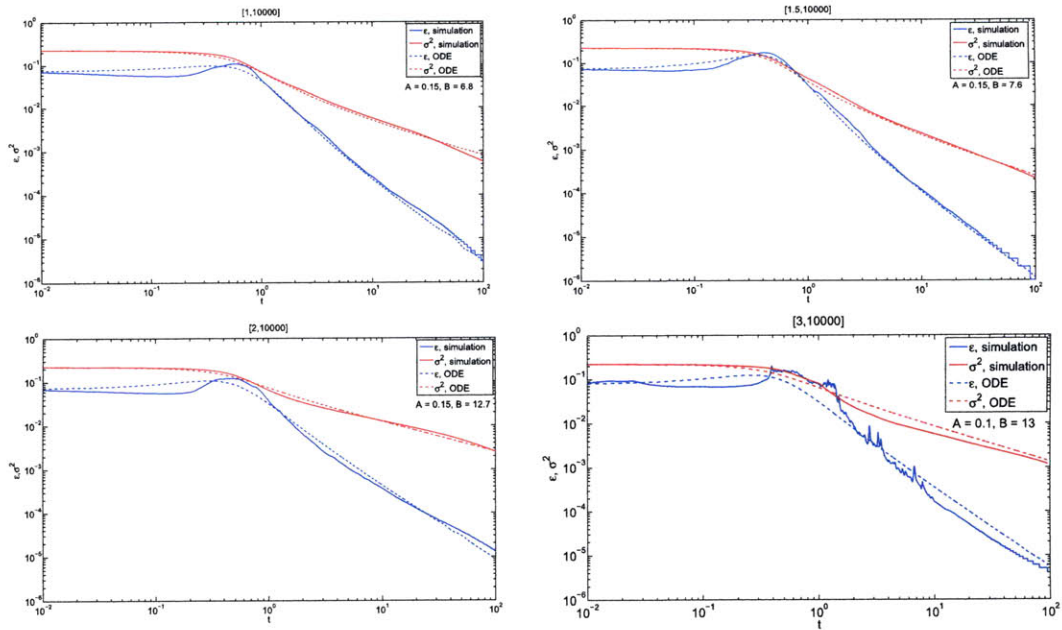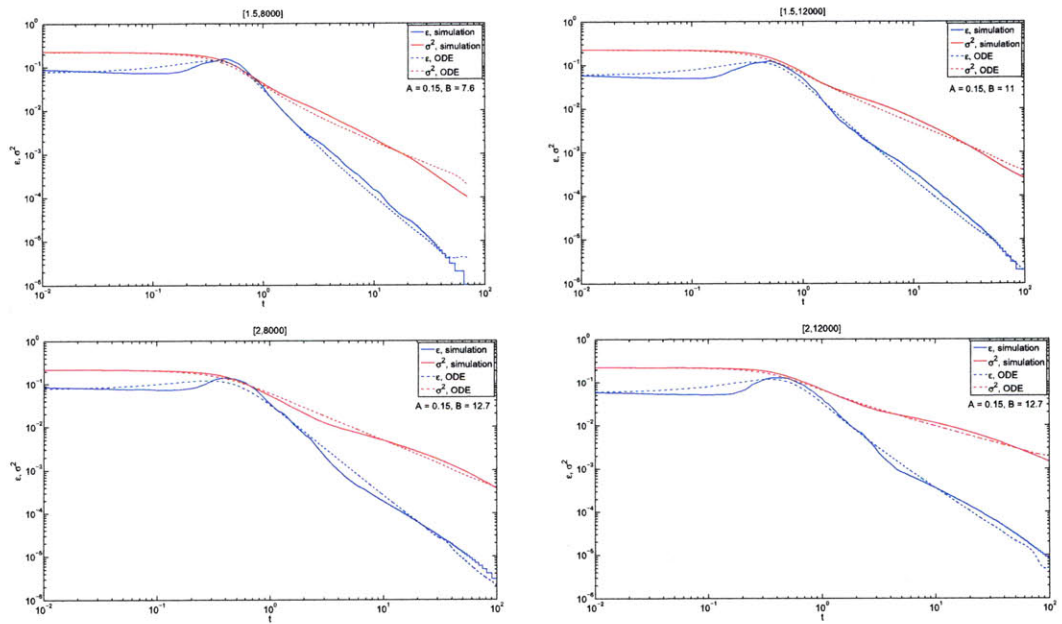

Figure 2-10: Mean dissipation rate and variance computed using the two-equation model compares well with the results from numerical simulations. Left plot shows results for $Pe = 8000$ and right plot shows results for $Pe = 12000$.
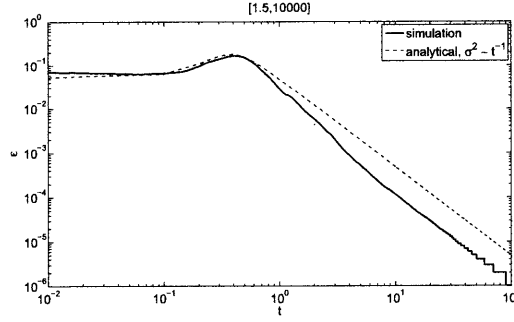
Figure 2-11: Mean dissipation rate computed from Eq. (2.49) with variance approximated as $\sigma^2 \sim t^{-1}$. The ODE for ϵ can still capture the characteristic hump and scaling of ϵ during viscous fingering.

the diffusive term which is controlled by the coefficient B. We also mention that at higher R, coefficients require more tuning.

We notice that at very early time, mean dissipation rate in simulation declines slightly before rising due to the viscous fingering effect. This decline is not captured by the ϵ equation in the proposed model which has only two terms - the rising term which dominates at early time and the decling term which dominates at late times. This early overestimation of ϵ in the model makes σ^2 lower so much so that it can only be matched if ϵ from the model is smaller than that from the simulation in the hump region. σ^2 reflects the area under the $\epsilon - t$ curve, thus mismatch in ϵ is carried over to σ^2 even at later times. In the figures above, we have attempted to achieve better match in σ^2, even if that required falling short on the magnitude of the hump. We emphasize σ^2 because it quantifies the degree of mixing.

2.3.1 Maximum of mean dissipation rate

In the time evolution of mean dissipation rate, $d\epsilon/dt = 0$ at the maximum ϵ. This gives,

$$\epsilon_{max} = \frac{A^2 Pe R^2 U^2 \sigma^4}{B^2} \tag{2.50}$$
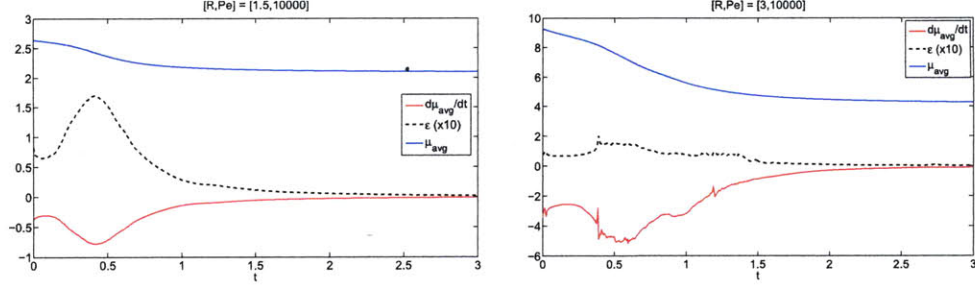
46

Figure 2-12: Evolution of average mixture viscosity, mean dissipation rate (multiplied by an arbitrary factor of 10) and rate of change in average mixture viscosity are the three curves plotted above. It clearly shows that the inflexion point in the average viscosity curve, which corresponds to a minimum in the $d\overline{\mu}/dt$, occurs at the same time as ϵ reaches its maximum.

Using Eq. (2.23), we obtain variance at ϵ_{max} as,

$$\sigma^2 = \left[\frac{1}{\sigma_0^2} + \frac{2\mathrm{A}^2 PeR^2U^2 t_{\mathrm{max}}}{\mathrm{B}^2}\right]^{-1} \tag{2.51}$$

Maximum ϵ also corresponds to $d\epsilon/d\sigma^2 = 0$ and minimum $d\overline{\mu}/dt$ or $d^2\overline{\mu}/dt^2 = 0$ (Fig. 2-14). As the less viscous fluid enroaches into the domain through fingering, average viscosity of the domain decreases. The rate of decrease is faster at early time and slower at later times, giving rise to an inflexion point in the evolution of the average viscosity. Since the changes in viscosity is due to the changes in interface length, ϵ and $d\overline{\mu}/dt$ are related. We will show it here.

Average mixture viscosity $\overline{\mu}$ can be expressed as,

$$\overline{\mu} = \frac{1}{A_t} \int_0^1 \mu dA, \tag{2.52}$$

where dA is the area enclosed by contours $c = c^* + \delta c^*$ and $c = c^*$. μ is the mixture viscosity inside dA and $A_t = 1$ is the total area of the domain. Now, since $A - \mu$ relation is one-to-one (right plot in Fig. 2-13) we can replace the integral in A with an equivalent integral in μ as follows,

$$\overline{\mu} = \frac{1}{A_t} \int_1^{e^R} A d\mu. \tag{2.53}$$

47

Now, differentiating with respect to time,

$$\frac{\mathrm{d}\overline{\mu}}{\mathrm{d}t} = \frac{1}{A_t} \int_1^{e^R} \frac{\partial A}{\partial t} \mathrm{d}\mu.$$ (2.54)

We need an expression for the evolution of the area enclosed by a concentration contour. Using Nakamura's effective diffusivity approach which relates changes in contour area to changes in total diffusive flux across the contour line (Eq. (A.14)), we obtain,

$$\frac{\mathrm{d}\overline{\mu}}{\mathrm{d}t} = -\frac{1}{A_t} \int_1^{e^R} \frac{\partial}{\partial c^*} \left(\epsilon^* \frac{\partial A}{\partial c^*} \right) \mathrm{d}\mu$$ (2.55)

Since $\mu(c) = e^{R(1-c)}$, we can write, $\mathrm{d}\mu = -R\mu \mathrm{d}c$,

$$\begin{aligned}
\frac{\mathrm{d}\overline{\mu}}{\mathrm{d}t} &= \frac{R}{A_t} \int_1^0 \mu \frac{\partial}{\partial c^*} \left(\epsilon^* \frac{\partial A}{\partial c^*} \right) \mathrm{d}c \\
&= -\frac{R}{A_t} \int_{c^*=0}^{c^*=1} \mu \mathrm{d} \left(\epsilon^* \frac{\partial A}{\partial c^*} \right) \\
&= -\frac{R}{A_t} \left[\left(\mu \epsilon^* \frac{\partial A}{\partial c^*} \right)_{\epsilon^*=0}^{\epsilon^*=0} - \int_{e^R}^1 \epsilon^* \frac{\partial A}{\partial c^*} \mathrm{d}\mu \right] \\
&= -\frac{R}{A_t} \int_0^1 \epsilon^* \frac{\partial A}{\partial c^*} R\mu \mathrm{d}c \\
&= -\frac{R^2}{A_t} \int_0^1 \mu \epsilon^* \mathrm{d}A \\
&\sim -\frac{R^2 \overline{\mu}}{A_t} \int_0^1 \epsilon^* \mathrm{d}A
\end{aligned}$$ (2.56)

Conditional dissipation rate ϵ^* is defined using Eq. (A.13) as,

$$\epsilon^* = \frac{1}{Pe} \frac{\partial}{\partial A} \int_{c \leq c^*} |\nabla c|^2 \mathrm{d}S = \frac{1}{Pe} \langle |\nabla c|^2 \rangle_{c^*}$$ (2.57)
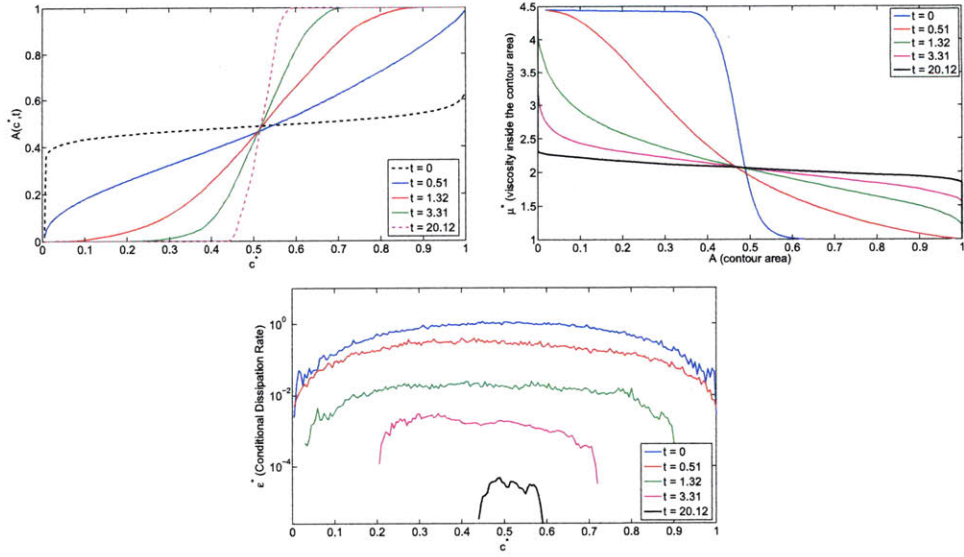
48

Figure 2-13: $A(c^*, t)$ is the area enclosed by the contour of $c = c^*$. As shown on the left figure, it is a monotonically increasing function of c as defined in Eq. (A.5) and it evolves in time due to mixing. Similarly, right figure shows that the relation between average viscosity and contour area is also one-to-one. Bottom figure shows that conditional dissipation rate is a non-monotonic function of concentration. $R = 1.5$, $Pe = 10000$ blobs simulation.

Integrating with respect to A,

$$
\begin{aligned}
\int_0^1 \epsilon^* \mathrm{d}A &= \frac{1}{Pe} \int_{c^*=0}^{c^*=1} \mathrm{d} \left(\int_{c \leq c^*} |\nabla c|^2 \, \mathrm{d}S \right) \\
&= \frac{1}{Pe} \left[\int_{c \leq c^*} |\nabla c|^2 \, \mathrm{d}S \right]_{c^*=0}^{c^*=1} \\
&= \frac{1}{Pe} \int |\nabla c|^2 \, \mathrm{d}S - 0 \\
&= A_t \epsilon
\end{aligned}
\tag{2.58}
$$

Hence, Eq. (2.56) becomes,

$$
\frac{\mathrm{d}\overline{\mu}}{\mathrm{d}t} \sim -R^2 \overline{\mu} \epsilon
\tag{2.59}
$$

Thus, we have shown that rate of decrease in mixture viscosity is directly proportional to the mean dissipation rate. Therefore, maximum ϵ corresponds to minimum $\mathrm{d}\overline{\mu}/\mathrm{d}t$.
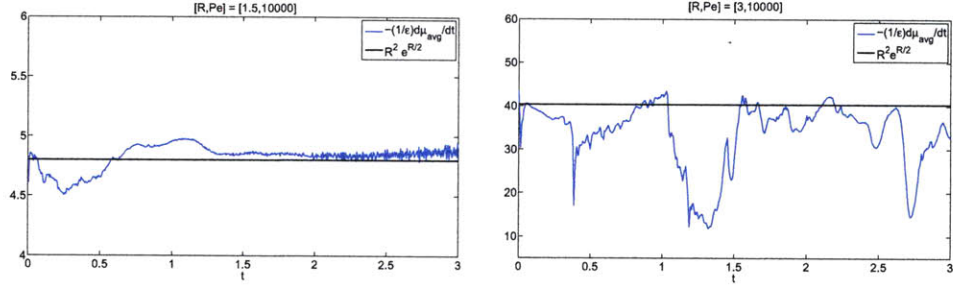
49

Figure 2-14: Verifying Eq. (2.59) for $R = 1.5, 3$. The relation obtained between mean dissipation rate and rate of decrease in mixture viscosity is approximately correct.

2.4 Effective diffusivity

The optimum in Pe can be understood through effective diffusivity. Diffusivity is modified due to stretching of the fluid interface. A stretched interface is thinner and has higher gradient across it. It also provides larger area for diffusive flux. Therefore, initially when Pe is increased and interface length increases, effective diffusivity increases until Pe reaches Pe_{opt}, then as Pe is increased further, which causes severe splitting, it increases the number of fingers but decreases their typical length. As a result, effective diffusivity decreases. With this argument, effective diffusivity has an optimum Pe and can be related to the mean dissipation rate because dissipation rate is directly related to the interface length.

It has been shown that an effective diffusivity can be computed for each concentration value, by rewriting the ADE using a coordinate transformation (using area of the concentration contour as a Lagrangian coordinate) (see the derivation in Appendix A.2, which is based on [26, 51]). This makes it possible to define an effective diffusivity D_{eff} as follows,

$$D_{\text{eff}} = D \frac{L_e^2(A, t)}{L_y^2} \tag{2.60}$$

Using the definition of conditional dissipation rate in Eq. (A.17), we have square of effective length as,

$$L_e^2(A, t) = \frac{\epsilon^* Pe}{(\partial c^* / \partial A)^2}. \tag{2.61}$$
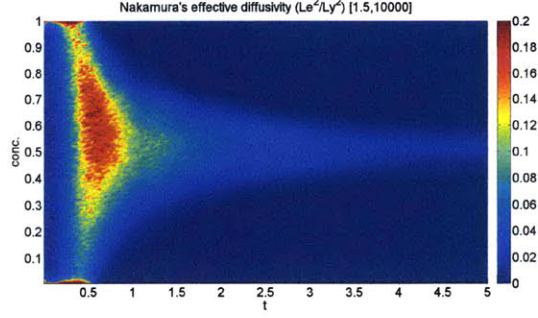
50

Figure 2-15: Effective diffusivity as a function of concentration. Red and blue colors denote high and low effective diffusivities, respectively. Each concentration value has its own effective diffusivity based on its contour length.

Hence the effective diffusivity becomes,

$$D_{\text{eff}} = \frac{UW}{Pe_{\text{eff}}} = \frac{\epsilon^*}{L_y^2 \left(\partial c^*/\partial A\right)^2}. \tag{2.62}$$

Maximum effective diffusivity corresponds to maximum mixing and, therefore, gives optimum Pe and optimum R. We see from Fig. 2-16 that effective diffusivity initially starts at a value determined by the initial configuration (initial interface length). Then it rises due to fingering and after reaching a maximum it declines under the influence of molecular diffusion which wipes out the interfaces. We also note that the maximum effective diffusivity in our blobs setup is obtained by $R = 1.5$ and $Pe = 10000$ which is indeed the simulation with fastest mixing.

The equivalent length, and hence the effective diffusivity, takes into account the enhancement to diffusion due to fingering which increases the length of concentration contours and influences the concentration gradients $\langle |\boldsymbol{g}| \rangle$ through a combination of fingering and mixing. The magnitude of the effective diffusivity is thus directly related to the geometric complexity of these contours. Generally, regions with relatively simple contours and small D_{eff} correspond to transport barriers and regions with a large D_{eff} are representative of mixing regions where the motion of fluid particles tend towards chaotic.
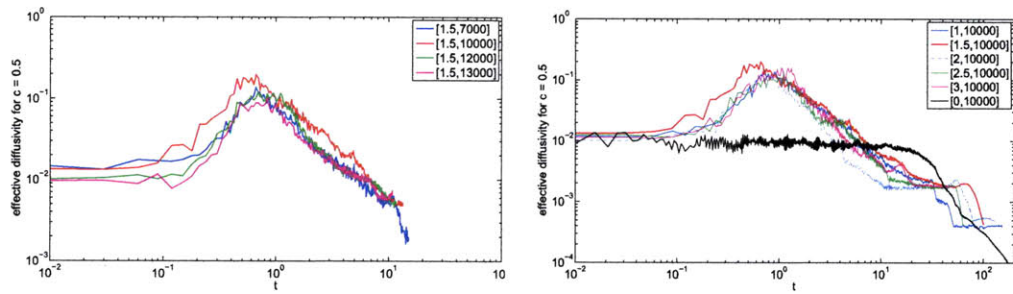
51

Figure 2-16: Left figure shows evolution of effective diffusivity for $c = 0.5$ contour at different Pe. Right figure shows the effective diffusivity at different R. Notice that initial value is approximately 0.01 which corresponds to the initial condition. Initially, we have about 16 blobs of radius 0.1 approximately which corresponds to a contour length, L_e, of 10 which gives $D_{\text{eff}} = \frac{L_e^2(A,t)}{L_y^2 Pe} = 0.01$. At very late time when fluid homogenizes and concentration reaches around 0.5, we loose all contours and L_e, and hence D_{eff}, tends to 0.

Chapter 3

# Viscous fingering simulations in a periodic domain

We perform periodic simulations under three settings: stripes (alternating longitudinal stripes of less and more viscous fluids inside a square domain), blobs (randomly distributed blobs of more viscous fluid inside a square domain filled with the less viscous fluid), and slab (a slug of less viscous fluid displacing more viscous fluid filled inside a rectangular domain). Below we describe each of these setups with the respective simulation results. We obtain scaling of dissipation length scale in a purely diffusive displacement ($R = 0$) and compare numerical simulation results with analytical results.

3.1 Stripes simulations in a square domain

We will first look at the evolution of ϵ in a purely diffusive mixing i.e. $R = 0$. We perform simulations in a square periodic domain filled with two fluids of equal viscosity initially distributed as alternating stripes of equal and uniform thickness. Flow is from left to right at reference dimensionless velocity of $U = 1$. We look at the evolution of s and ϵ for different stripe thicknesses. Since $\frac{\partial}{\partial x}$ terms are zero with
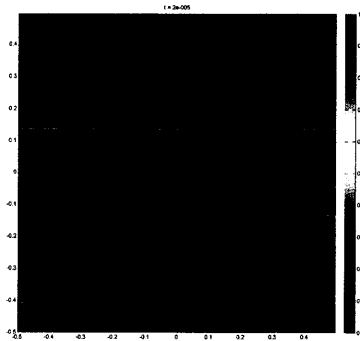
(A) $t = 0$, stripe thickness=0.09
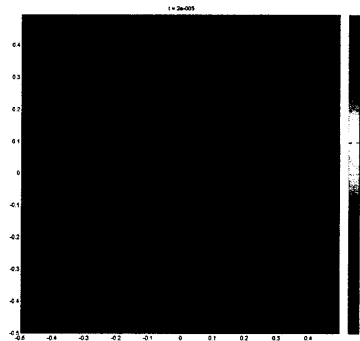
(B) $t = 0$, stripe thickness=0.2

Figure 3-1: Initial concentration fields in stripes simulations with two different stripe thicknesses. $[R, Pe] = [0,10000]$.
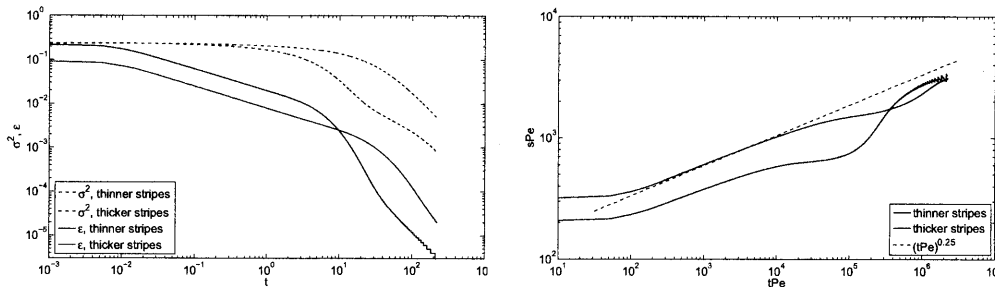

Figure 3-2: Left figure compares σ^2 and ϵ from the two simulations of different stripe thicknesses. Right figure compares s from the same two simulations. Notice the diffusive scaling, $\epsilon \sim t^{-1/2}$ and $s \sim t^{1/4}$. Notice that ϵ for thicker stripes is smaller than that in the thinner stripes because of a smaller total interface length (fewer stripes initially). Since σ_0^2 is same between these two initial conditions, s starts at higher value for the thicker stripes simulation. However, because the 'finger width' is smaller in case of thinner stripes, it takes less time to diffuse across one stripe thickness. Therefore, the exponential drop in ϵ starts earlier in case of thinner stripes. As a result, s in the thinner stripes simulation starts to grow faster, sooner than the thicker stripes case, and eventually catches up.

this intial condition, Eq. (1.1) becomes,

$$\frac{\partial c}{\partial t} = \frac{1}{Pe}\frac{\partial^2 c}{\partial y^2} \tag{3.1}$$

Eq. (3.1) has an analytical solution under these simple initial and boundary conditions,

$$\begin{aligned}
c(y,t) = 1 + 0.5\bigg[&\mathrm{erf}\left(\frac{y+0.1}{2}\sqrt{\frac{Pe}{t}}\right) - \mathrm{erf}\left(\frac{y-0.1}{2}\sqrt{\frac{Pe}{t}}\right) \\
&- \mathrm{erf}\left(\frac{y+0.3}{2}\sqrt{\frac{Pe}{t}}\right) + \mathrm{erf}\left(\frac{y-0.3}{2}\sqrt{\frac{Pe}{t}}\right)\bigg]
\end{aligned} \tag{3.2}$$

which gives,

$$\begin{aligned}
\frac{\partial c}{\partial y} = \frac{\sqrt{Pe}}{2\sqrt{\pi t}}\bigg[&\exp\left(-\frac{Pe(y+0.1)^2}{4t}\right) - \exp\left(-\frac{Pe(y-0.1)^2}{4t}\right) \\
&- \exp\left(-\frac{Pe(y+0.3)^2}{4t}\right) + \exp\left(-\frac{Pe(y-0.3)^2}{4t}\right)\bigg]
\end{aligned} \tag{3.3}$$

which, using Eq. (2.12), becomes,

$$\epsilon = \frac{1}{Pe}\frac{1}{V}\int\left(\frac{\partial c}{\partial y}\right)^2 \mathrm{d}V \tag{3.4}$$

We find $\epsilon \sim t^{-1/2}$. We can also obtain an evolution equation for ϵ from Eq. (2.32). With constant and uniform velocity field $\boldsymbol{U} = (1, 0)$,

$$\frac{\mathrm{d}\epsilon}{\mathrm{d}t} + \frac{2}{Pe^2}\sum_i\langle|\nabla g_i|^2\rangle = 0 \tag{3.5}$$

or,

$$\frac{\mathrm{d}\epsilon}{\mathrm{d}t} + \frac{2}{Pe^2}\frac{1}{V}\int\left(\frac{\partial^2 c}{\partial y^2}\right)^2 \mathrm{d}V = \frac{\mathrm{d}\epsilon}{\mathrm{d}t} + \frac{2}{V}\int\left(\frac{\partial c}{\partial t}\right)^2 \mathrm{d}V = 0, \tag{3.6}$$

which gives the same scaling $\epsilon \sim t^{-1/2}$. We obtain the same scaling if stripes were along y (not shown here) instead of being along x. Fig. 3-3 shows that analytical results compare well with the numerical simulation.

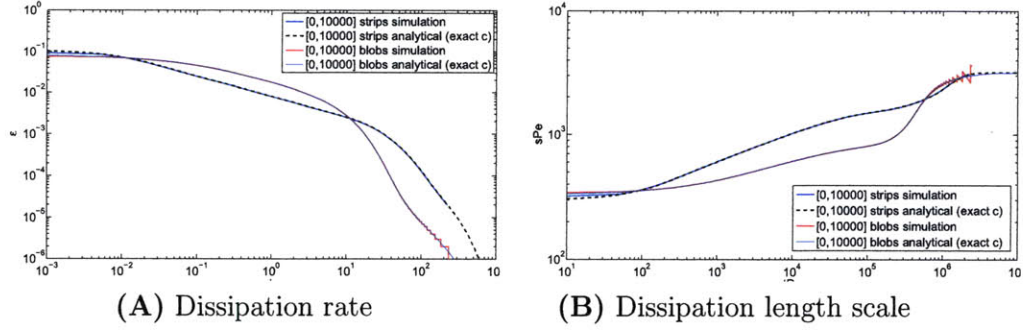**(A)** Dissipation rate   **(B)** Dissipation length scale

Figure 3-3: Analytically derived mean dissipation rate and dissipation length scale for $R = 0$ and $Pe = 10000$ in stripes simulation agrees with numerical simulations.

We can relate evolution in dissipation rate to the evolution of variance and dissipation length through Eq. (2.10) and Eq. (2.23). Let's take $\epsilon = C_1/(C_2 + \sqrt{t})$, where C_1, C_2 are small positive constants and initial dissipation rate is $\epsilon_0 = C_1/C_2$. Integrating Eq. (2.23) in time gives variance as,

$$\sigma^2 = \sigma_0^2 - 4C_1 \left[\sqrt{t} - C_2 \log \left(C_2 + \sqrt{t} \right) \right] \tag{3.7}$$

where σ_0^2 is the initial variance. Hence slope of $\sigma^2 - t$ curve is,

$$\frac{d\sigma^2}{dt} = \frac{-2C_1}{C_2 + \sqrt{t}} = -2\epsilon. \tag{3.8}$$

Since $C_1, C_2 \ll 1$, the slope decreases with time as $-t^{-0.5}$ and σ^2 is approximately constant at σ_0^2. It is interesting to look at the slope in $\sigma^2 - \epsilon$ plot,

$$\frac{d\sigma^2}{d\epsilon} = 4t + 4C_2\sqrt{t} = 4C_1 \frac{\sqrt{t}}{\epsilon}. \tag{3.9}$$

Hence the slope increases almost linearly with time (first RHS) as also seen in Fig. 3-15. This is true for $R = 0$. For scaling of s, we differentiate (2.10) to obtain,

$$s\frac{ds}{dt} = \frac{1}{2Pe} \left[\frac{d\sigma^2}{\epsilon dt} - \frac{\sigma^2}{\epsilon^2} \frac{d\epsilon}{dt} \right], \tag{3.10}$$

56

$$\frac{t\,ds}{s\,dt} = \frac{1}{2}\left[\frac{t}{\sigma^2}\frac{d\sigma^2}{dt} - \frac{t}{\epsilon}\frac{d\epsilon}{dt}\right],$$ (3.11)

$$\frac{d\log s}{d\log t} = \frac{1}{2}\left[\frac{d\log\sigma^2}{d\log t} - \frac{d\log\epsilon}{d\log t}\right].$$ (3.12)

For $R = 0$, since $\epsilon \sim t^{-1/2}$, hence,

$$\frac{d\log s}{d\log t} \sim \frac{1}{2}\frac{d\log\sigma^2}{d\log t} + \frac{1}{4}$$ (3.13)

First term on RHS is of the order of $O(10^{-3})$ at early times, hence $s \sim t^{1/4}$ (Fig. 3-2). After a certain time, when the $c = 1$ fluid disappears (can be seen in the PDF of c), ϵ starts to drop very fast resulting in faster increase in s. At late times, when fluids homogenize and concentration gradients disappear, dissipation rate becomes nearly zero and s asymptotes to a value determined by the dimensions of the domain.

3.2 Blobs simulation in a square domain

To focus on the evolution of finger coarsening process, we conduct viscous fingering simulations in a square domain filled with blobs of the less viscous fluid in a background of the more viscous fluid (Fig. 3-5, Fig. 3-6). We compute dissipation length scale, s, from simulations of different R and Pe under this setting (Fig. 3-10). Since the available length for fingering is reduced to the diameter of a blob, nonlinear interactions such as splitting, branching etc. are suppressed and, therefore, the evolution of s is different in a blobs simulation than in a slab simulation inside a longer domain. The optimum R, corresponding to a balance between number of fingers and their length, requires reaching smallest s in shortest time. This optimum R for blobs simulation is 1.5 (Fig. 3-13). It is around 2.25 for alternating-injection simulations in a 5:1 rectangular domain. We can observe this by comparing concentration field snapshots from Fig. 3-7 and Fig. 3-6 around $t = 0.51$, which corresponds to the time for minimum s (Fig. 3-12).

Evolution of dissipation length scale can be understood from the evolution of σ^2

(A) $t = 0$ **(B)** $t = 0.51$
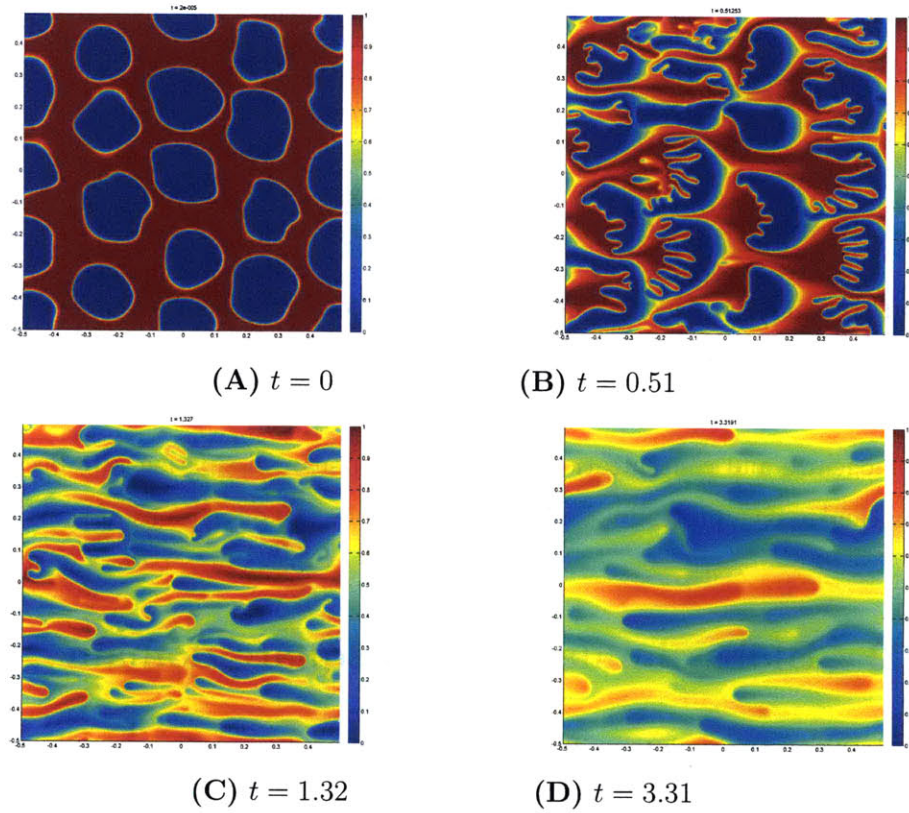
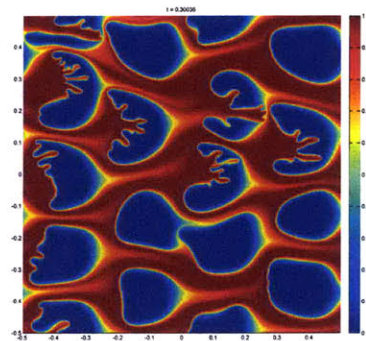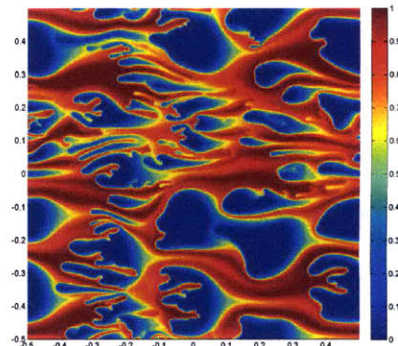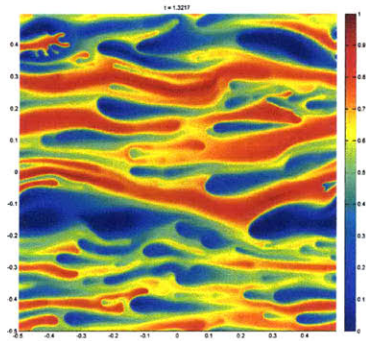**(C)** $t = 1.32$ **(D)** $t = 3.31$

Figure 3-4: Snapshots of concentration fields from blobs simulation $[R, Pe] = [1, 10000]$ in a periodic domain at four successive time steps. Top left figure is the initial concentration field. Except for the exact locations and shapes of the blobs, which are randomized, the initial condition is same for all the blobs simulations. Only the differ among simulations because they are randomized. Notice the growth of fingers inside each blob. These fingers merge, split and eventually disapper due to diffusive mixing with details of the their evolution depending on the R and Pe. We want to achieve highest interfacial area between the fluids during the fingering process which is dominant only at early times. Since the number of fingers and their typical longitudinal length are not directly propotional, highest interfacial area or maximum effective diffusivity corresponds to finding a balance between these two quantities. This balance is obtained at an optimum R and optimum Pe. $R = 1$ is our baseline simulation. We will continue to increase R (figures below) in the search for faster mixing conditions.
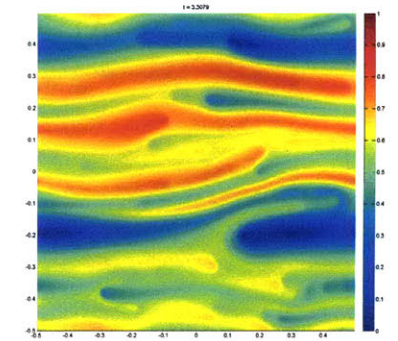
(A) $t = 0.30$

(B) $t = 0.51$

(C) $t = 1.32$

(D) $t = 3.31$

Figure 3-5: Snapshots of concentration fields from blobs simulation $[R, Pe] = [2, 10000]$ in a periodic domain at four successive time steps. Notice the signs of channeling as less viscous fluid tries to flow preferentially without contacting the other fluid. The less viscous fluid bypasses the more viscous fluid which is trapped in slow-moving islands or regions of poor mixing in the domain. This is a result of nonlocal coupling between the pressure field and the concentration field. It creates heterogeneous flow even in a homogeneous medium. Since channeling indicates high tip velocities and high R, $R = 2$ is too high to achieve optimum mixing in the blobs setup.
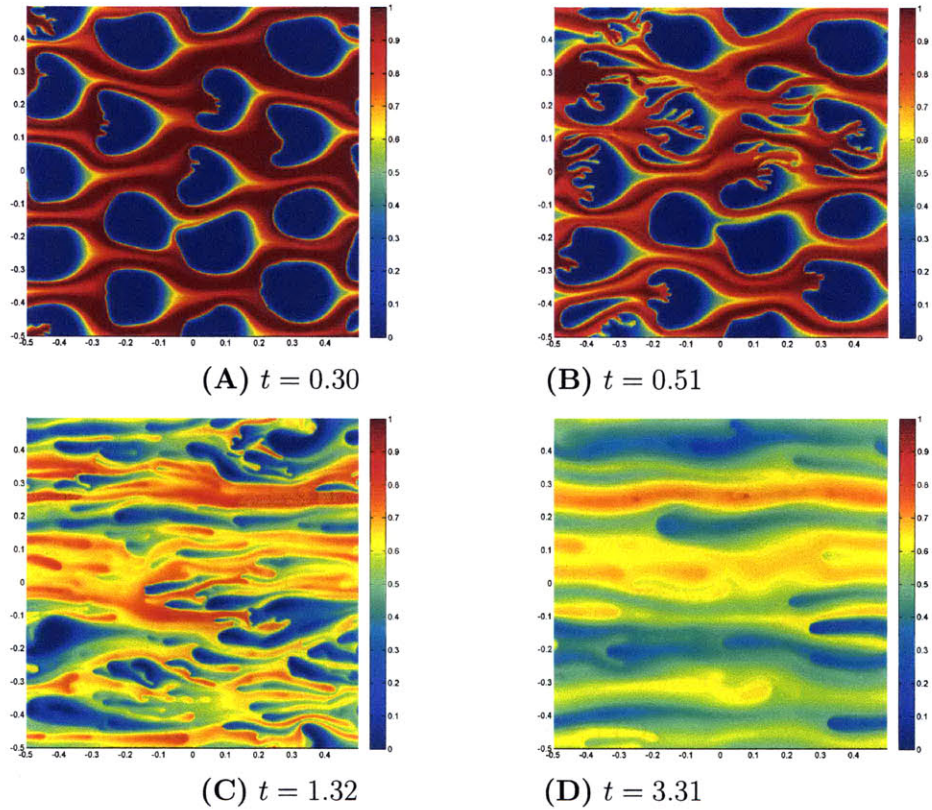
(A) $t = 0.30$

(B) $t = 0.51$

(C) $t = 1.32$

(D) $t = 3.31$

Figure 3-6: Snapshots of concentration fields from blobs simulation $[R, Pe] = [3, 10000]$ in a periodic domain at four successive time steps. Finger tip velocity has increased further. This results in formation of fewer and longer fingers that show clear signs of channeling. Also, some tip-splitting can be seen **(B)** which does not grow long because of the limited size of the blob. Overall, it appears that R is too high and the interface length can be increased by decreasing R.

(A) $t = 0.30$

(B) $t = 0.51$

(C) $t = 1.32$
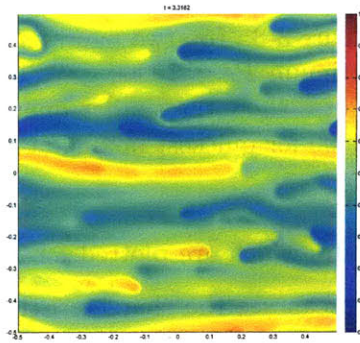
(D) $t = 3.31$

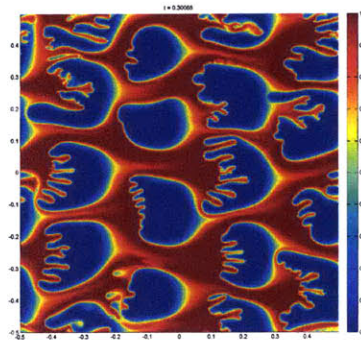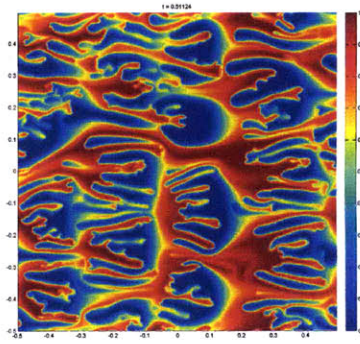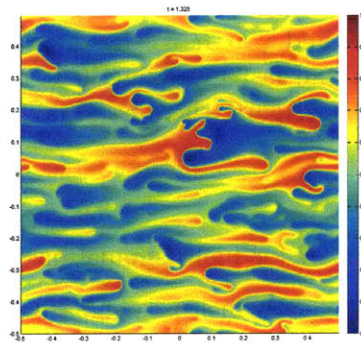Figure 3-7: Snapshots of concentration fields from blobs simulation $[R, Pe] = [1.5, 10000]$ in a periodic domain at four successive time steps. Notice that interface length should be maximum at $t = 0.51$. Comparing with snapshots at different R (Fig. 3-4, Fig. 3-5 and Fig. 3-6), $R = 1.5$ appears to create maximum interface length between the fluids for diffusive mixing to take place. Therefore, $R = 1.5$ should be the optimum R for mixing in this setup. From degree of mixing, χ, shown below, we conclude that indeed $R = 1.5$ is the optimum R.

(A) $R = 1$ **(B)** $R = 1$

(C) $R = 1.5$ **(D)** $R = 1.5$

Figure 3-8: Top two figures show evolution of ϵ and χ at $R = 1$ for different Pe. The optimum $Pe = 10000$ gives largest hump in ϵ and fastest mixing in χ. Bottom two figures show the similar quantities for $R = 1.5$. Again, there is an optimum Pe of 10000 for quickest mixing at $R = 1.5$.
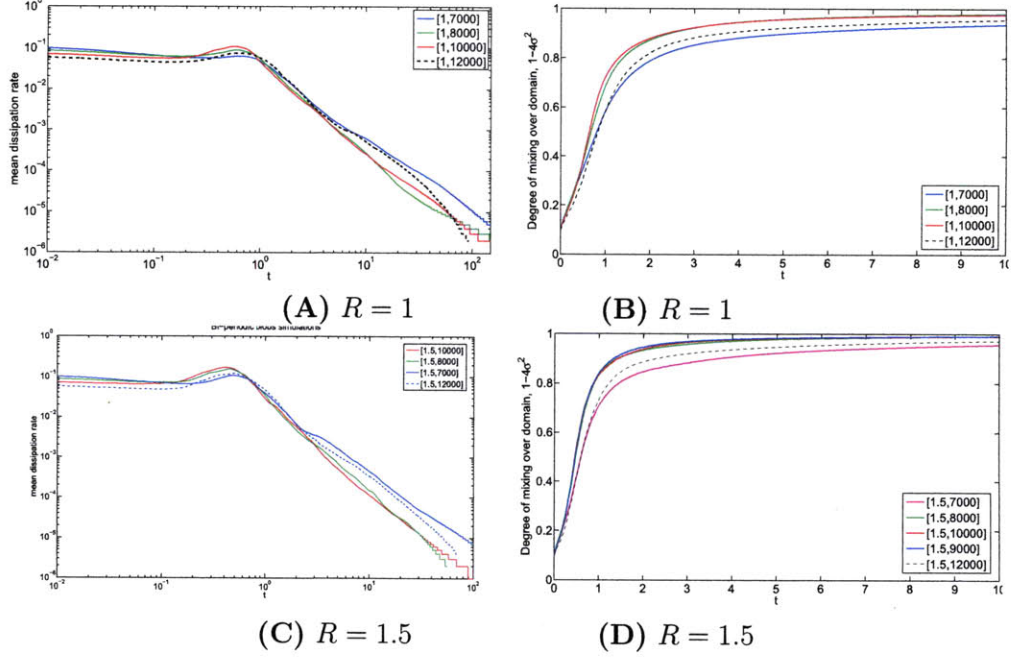
and ϵ which are plotted for $R = 1.5$ (optimum R for blobs simulation) in Fig. 3-9. We can see the characteristic hump in ϵ (Fig. 3-8) which is a signature of viscous fingering.

Let's derive the exact results for blobs simulation at $R = 0$. Eq. (3.1) becomes,

$$\frac{\partial c}{\partial t} + \frac{\partial c}{\partial x} = \frac{1}{Pe}\left(\frac{\partial^2 c}{\partial x^2} + \frac{\partial^2 c}{\partial y^2}\right) \tag{3.14}$$

which can be solved by Fourier Transform in x and y,

$$\tilde{c}(k_x, k_y, t) = \tilde{c}_0(k_x, k_y) \exp\left(-(k_x^2 + k_y^2 + ik_x Pe)\frac{t}{Pe}\right) \tag{3.15}$$

where $\tilde{c}$ and $\tilde{c}_0$ are Fourier Transforms of c and c_0 (initial condition), and k_x, k_y are wavenumbers in space. $c(x, y, t)$ can easily be obtained by inverse Fourier Transform of Eq. (3.15) using spatial periodicity. There is good agreement between numerical
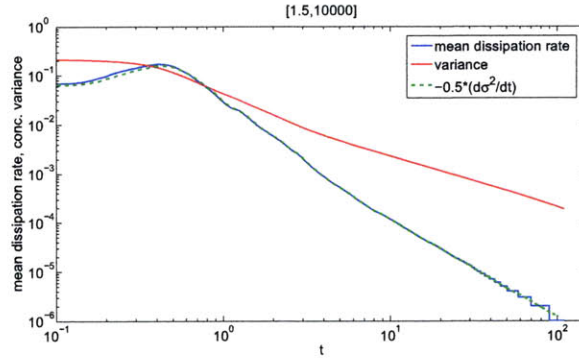
Figure 3-9: Mean dissipation rate is the rate of decay in variance as expressed in Eq. (2.24). Figure shows excellent agreement between ϵ and negative slope of σ^2.

(A) $R = 1$ **(B)** $R = 2$
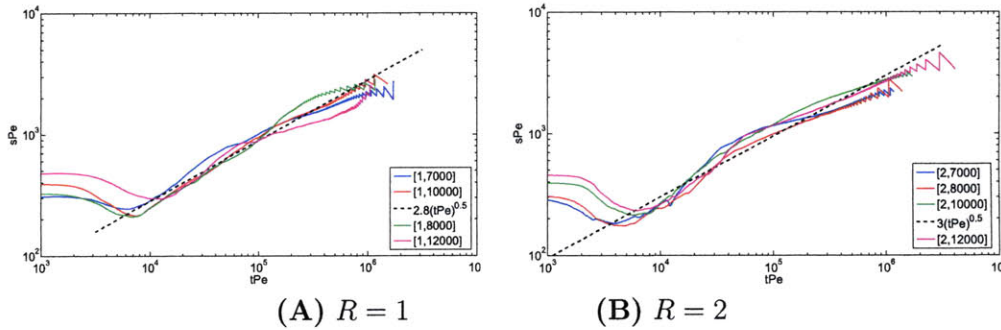
Figure 3-10: Dissipation length scale, s, as a global measure of coarsening during viscous fingering. Notice that in the beginning s scales as $Pe^{-1/2}$, then it dips due to fingering and then it increases due to diffusion. The dip reflects the stretching of material interface due to fingering. At lower Pe of 8000, fewer fingers form but can grow longer because they are wider. At high Pe of 10000, lots of tiny fingers emerge but they diffuse faster than they can grow in length. At $Pe = 7000$, diffusion is too strong to allow growth in finger length and hence it is outside the optimum Pe range for $R = 1$. For $R = 2$, the largest dip in s corresponds to $Pe = 8000$. $Pe = 10000$ is out of optimum Pe range.
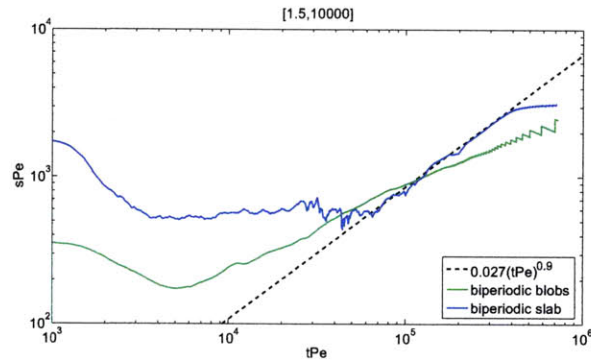
Figure 3-11: Evolution of s in a blobs simulation is different from that in a slab simulation. In the slab simulation inside a longer 5:1 domain, the stretching of interface due to fingering can continue for longer duration during which time $\epsilon \sim t^{-0.5}$ which is the purely diffusive scaling obtained earlier. Since σ^2 is monotonically decreasing with time, so $s \sim \frac{\sigma}{\langle |g| \rangle}$ remains almost flat for this duration. When the less viscous fluid disappears, ϵ starts to drop quickly and s starts to rise quickly.
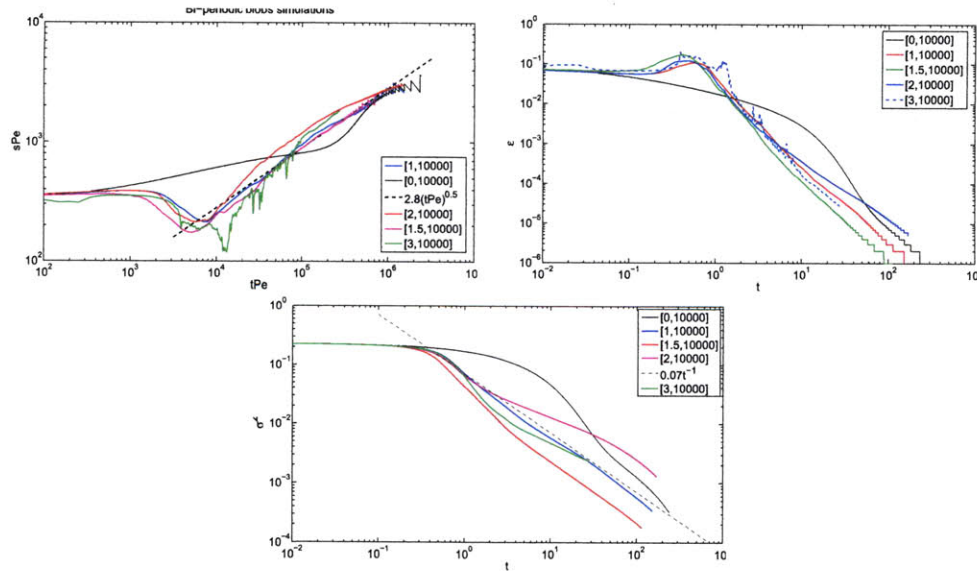
Figure 3-12: The three figures show evolution of sPe, ϵ, and σ^2 for simulations with different R at $Pe = 10000$. Notice the dip in s corresponding to the hump in ϵ for $R > 0$. Magnitude of the earliest and largest dip in $s - t$ graph or hump in $\epsilon - t$ graph can identify optimum R for mixing.

64
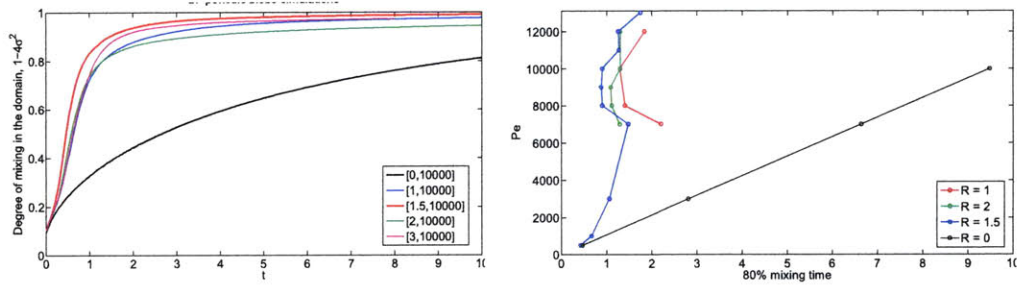
Figure 3-13: Left plot shows evolution of degree of mixing for different R. Optimum R corresponds to minimum time taken to achieve a desired degree of mixing (say 0.8) and can be read from this plot. The time taken to achieve a desired degree of mixing is known as mixing time. Right plot shows increase in this mixing time as Pe is increased, for different R. Optimum Pe at a given R corresponds to the minimum mixing time. Notice that mixing time increases linearly for $R = 0$, as expected. From these plots, optimum $[R, Pe]$ for blobs in a square domain is around $[1.5, 9000]$ at which number of fingers and their length balance to create maximum interface area over which diffusive mixing can take place. We reach at the same conclusion by looking at the snapshots of concentration field from different simulations.
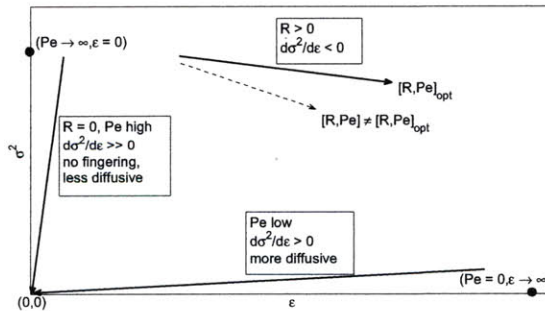
Figure 3-14: In the $\sigma^2 - \epsilon$ plot we can identify three characteristic regions. Effect of viscous fingering is easily seen in the slope. $\epsilon_{\max}$ corresponds to $d\epsilon/d\sigma^2 = 0$.

(A) $Pe = 7000$ **(B)** $Pe = 8000$

(C) $Pe = 10000$ **(D)** $R = 1.5$
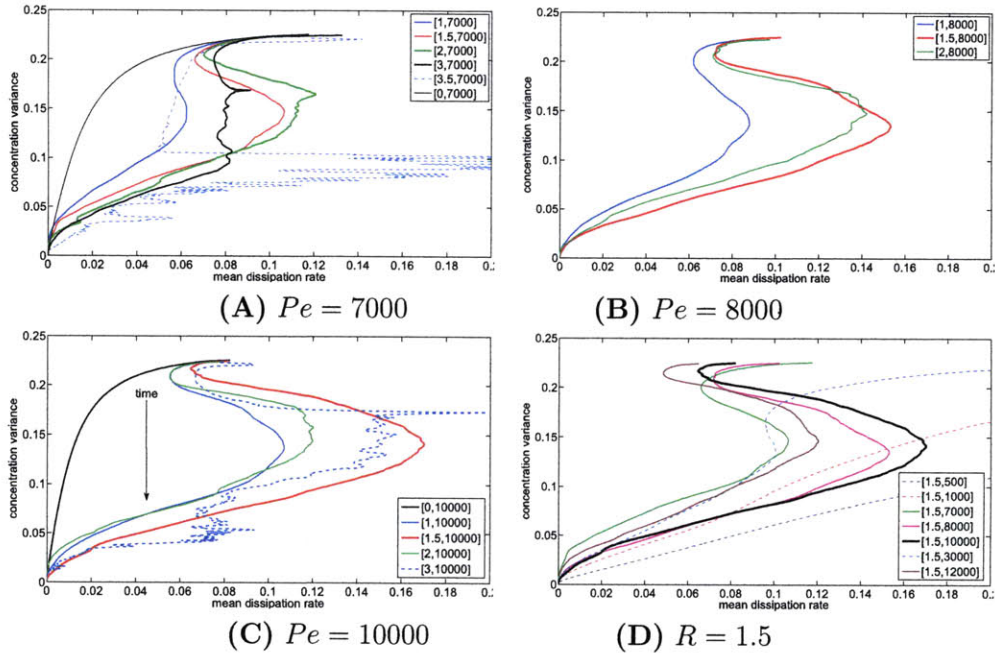
Figure 3-15: $\sigma^2 - \epsilon$ plot highlights the optimum $[R, Pe]$ for mixing. First three figures show σ^2 as a function of ϵ for three different Pe, with each figure showing the effect of variation in R at that Pe. The R with maximum and earliest hump in ϵ decreases from 2 to 1.5 as Pe is increased from 7000 to 10000. Fourth figure on bottom right shows the effect of Pe at $R = 1.5$. Notice that the curve moves to left as Pe increases from 500 to 3000 and then it moves to right as Pe in increased further. $Pe = 3000$ marks the boundary beyond which viscous fingering becomes dominant during early time evolution. The hump starts to appear at $Pe = 3000$ and keeps growing until $Pe = 10000$, after which it decreases for $Pe = 12000$. Hence, $Pe = 10000$ marks the maximum effective diffusivity at $R = 1.5$. Note that in **(D)**, because of fingering-induced hump at higher Pe, evolution of ϵ subsequent to the hump is very similar to that in a system with very low Pe. This indicates an increase in effective diffusivity with Pe due to viscous fingering.
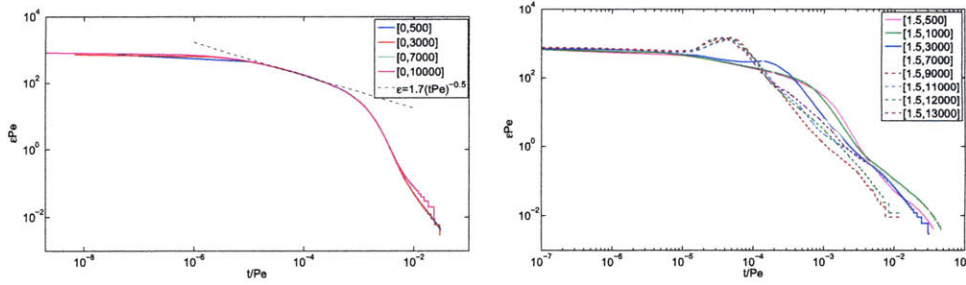
Figure 3-16: Diffusive scaling collapses curves for different Pe in the diffusive regime only. Left figure shows that ϵ from different Pe simulation at $R = 0$ can be collapsed into one single curve with appropriate scaling (note the axis labels). Right figure applies the same scaling at $R = 1.5$ and we find that it did not collapse the curves except at early time.
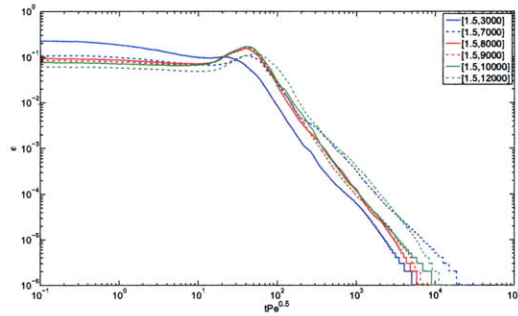
Figure 3-17: Rescaling time as $t\sqrt{Pe}$ aligns the hump in ϵ for different Pe.

simulation results and these analytical results (Fig. 3-3).

We can collapse $\epsilon - t$ curves for different Pe to a single curve by plotting ϵPe against t/Pe as in Fig. 3-16. The $\sqrt{Pe}$ factor in the advective term of Eq. (2.49) indicates we can align the hump in $\epsilon - t$ curves for different Pe by scaling time as $t\sqrt{Pe}$, i.e.,

$$\frac{d\epsilon}{d(t\sqrt{Pe})} - \mathrm{A}RU\epsilon^{3/2} + \mathrm{B}\frac{\epsilon^2}{\sqrt{Pe}\sigma^2} = 0, \qquad (3.16)$$

Since variance also changes with Pe, non-monotonically, this rescaling of time does not collapse $\epsilon - t$ for all Pe (Fig. 3-17).

It is useful to look at the Fourier spectrum of the concentration field as mixing evolves (Fig. 3-18). We notice that the decay of Fourier amplitudes is faster with time as expected in a purely decaying process.

67
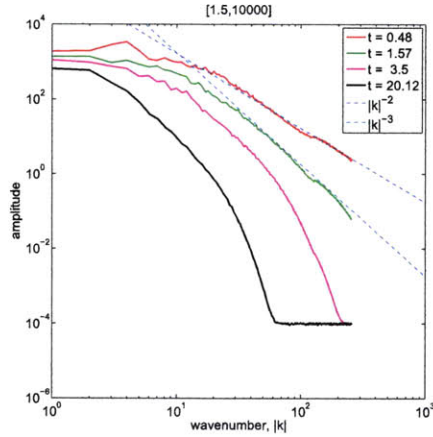
Figure 3-18: Fourier spectrum of concentration for $R = 1.5$, $Pe = 10000$. Notice the continuous increase in the decay exponent because it is a purely decaying setup.

3.3 Slab simulation in a rectangular domain

We conduct simulations of displacement of the more viscous fluid by a slab of less viscous fluid in a rectangular periodic domain. The idea is to allow fingering for longer duration as the slab moves along the length of this 5:1 (length-to-width) domain.

The optimum R for this setup is different because the homogeneous mixture concentration is not $c = 0.5$ but $c = 0.2$. Therefore, the average mixture viscosity $(\sim e^{0.8R})$ is higher:
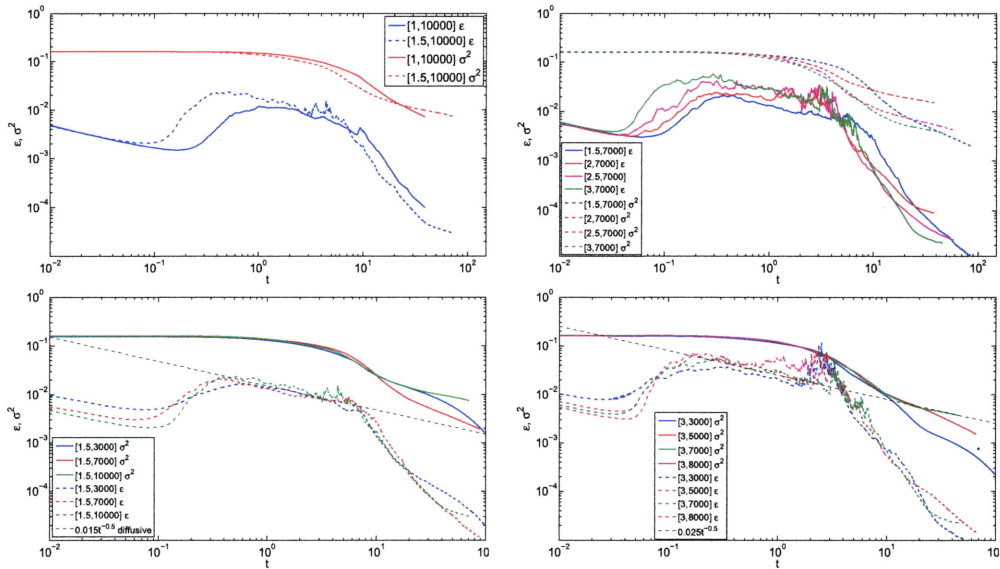
Figure 3-19: Top two figures show evolution of ϵ and σ^2 in a slab setup at $Pe = 10000$ and $Pe = 7000$. Within each of these two figures, effect of R is investigated. Bottom two figures show same quantities at two different R with each figure investigating the influence of Pe at that particular R. The hump in ϵ becomes broader in the slab simulation as stretching of the interface continues for longer duration. During this time, evolution of ϵ follows purely diffusive scaling (dotted straight line). Results are slightly affected from numerical errors between $t = 2$ and $t = 3$ when the slug crosses right boundary for the first time.
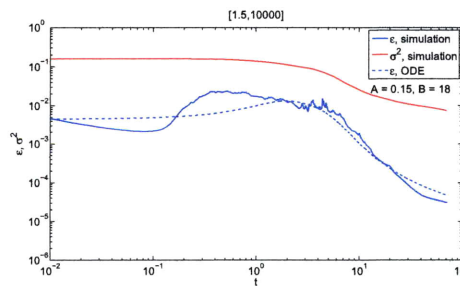
Figure 3-20: ϵ by solving Eq. (2.49), with σ^2 taken from the simulation, does not capture the entire behaviour of ϵ from the direct numerical simulation. Especially, the early time diffusive decline is missed because the rising term, with $\epsilon^{3/2}$ in Eq. (2.49), dominates.

69

Chapter 4

Alternating-injection simulations

Mixing in alternating injection viscous fingering displacements is a combined result of three different forcings:

1. Viscous fingering - Channelling, splitting, branching, merging etc. directly influences concentration gradients and interfacial area between the fluids. Mixing is a function of this interfacial area. In case of alternating injection, fingers have the potential to connect successive slugs of less viscous fluid across the span of a more viscous slug. This promotes mixing. R and Pe control the strength of viscous fingering.

2. Diffusion - Diffusion tends to wipe out sharp gradients in concentration field. In transverse direction it increases the width of the finger and thereby mixing but at the cost of slowing down the longitudinal growth of the finger thus leading to a slower mixing at the outlet. Pe determines the strength of diffusive forces.

3. Alternating injection boundary - Time periodicity of the flow attempts to create a chaotic advection like environment to enhance the interaction between the two fluids and thereby mixing. Frequency and slug ratio will determine the strength of this oscillatory forcing.

It seems reasonable to separate the influence of each of these forcings. Therefore, we conduct a range of simulations where R and Pe are varied and we also conduct simulations with single slug in a periodic domain as described in the previous chapter.

(A) $[R, Pe, t] = [3{,}5000{,}2.43]$ **(B)** $[R, Pe, t] = [6{,}1000{,}2.69]$

(C) $[R, Pe] = [5{,}5000{,}2.58]$ **(D)** $[R, Pe, t] = [6{,}2000{,}12.42]$
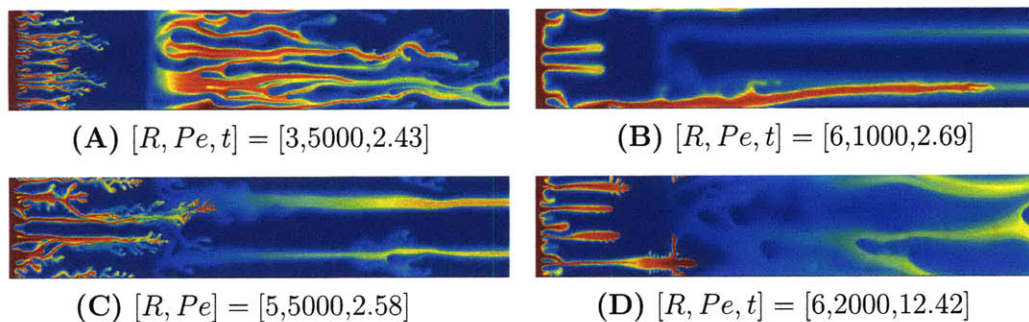
Figure 4-1: Snapshots of concentration fields from alternating-injection simulations highlighting nonlinear interactions among viscous fingers. There are two slugs of less viscous fluid (red) shown in each figure-one is leaving the from the right edge and the other is entering from the left edge. Notice tip-splitting and fading **(A)**, channeling and shielding **(B)**, splitting, channeling and fading **(C)**. Notice suppression of Taylor dispersion near the tip and chaneling induced branching even at late times and relatively low Pe **(D)**. Concentration of less viscous fluid goes from 0 (blue) to 1 (red).

We perform numerical simulations for R ranging from 0 to 6 and Pe ranging from 100 to 7000 with selected increments. Fig. 4-1 shows snapshots of concentration field from simulations at different R and Pe. Aspect ratio of the domain is $L : W = 5 : 1$. Fig. 4-2 shows degree of mixing (χ) computed at the outlet as a function of time for various R and Pe. We can see that mixing increases with time, has an oscillatory behaviour and reaches a pseudo-steady state after 3 to 4 cycles of alternating injection. The time to reach this pseudo-steady state varies with R and Pe. Mixing time can be defined as the time for χ to reach a desired value, say 0.8.

It is interesting to note that sensitivity of mixing time to Pe is larger at high R (Fig. 4-3). This is a point of departure from globally chaotic mixing where mixing time is almost always insensitive to Pe ($t \sim \log Pe$), at high Pe. The answer again lies in the nonlinear, nonlocal coupling between velocity and concentration fields in case of viscous fingering displacements. At high R and high Pe, fingers start to display both channeling (and chaneling induced effects) and vigorous splitting primarily on the sides.

With evolution of χ from different $[R, Pe]$ simulations, we can plot optimum R as a function of Pe (Fig. 4-4), where optimum R gives minimum mixing time for
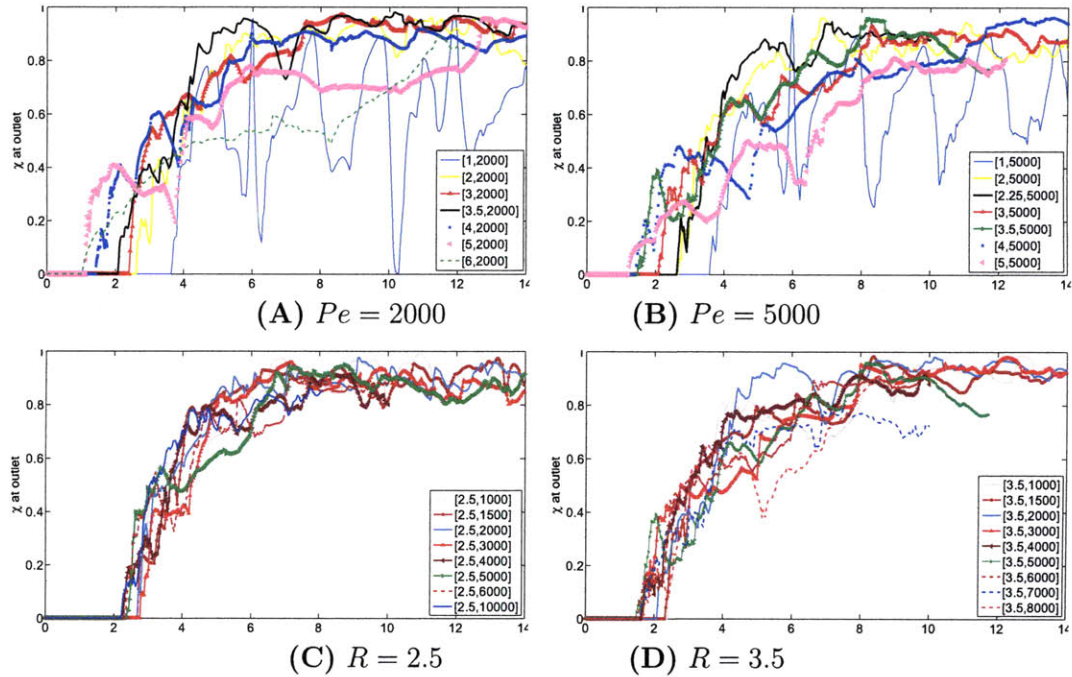
Figure 4-2: Degree of mixing from the numerical simulations of Eq. (1.1), for different values of R and Pe. Increasing R (**(A)** and **(B)**) has a non-monotonic impact on mixing time with large impacts near the extremes i.e. at low and high R. There is an optimum range of R that gives faster mixing and this range weakly depends on Pe. Notice that mixing starts to increase from 0 at smaller t as R gets larger because of the increasing tip velocity. Mixing time appears less sensitive to changes in Pe (**(C)** and **(D)**) especially for R near the optimum R range which is 2–3 for alternating injection setup.

73

(A) $R = 4$ **(B)** $R = 4.5$

(C) $R = 5$ **(D)** $R = 6$
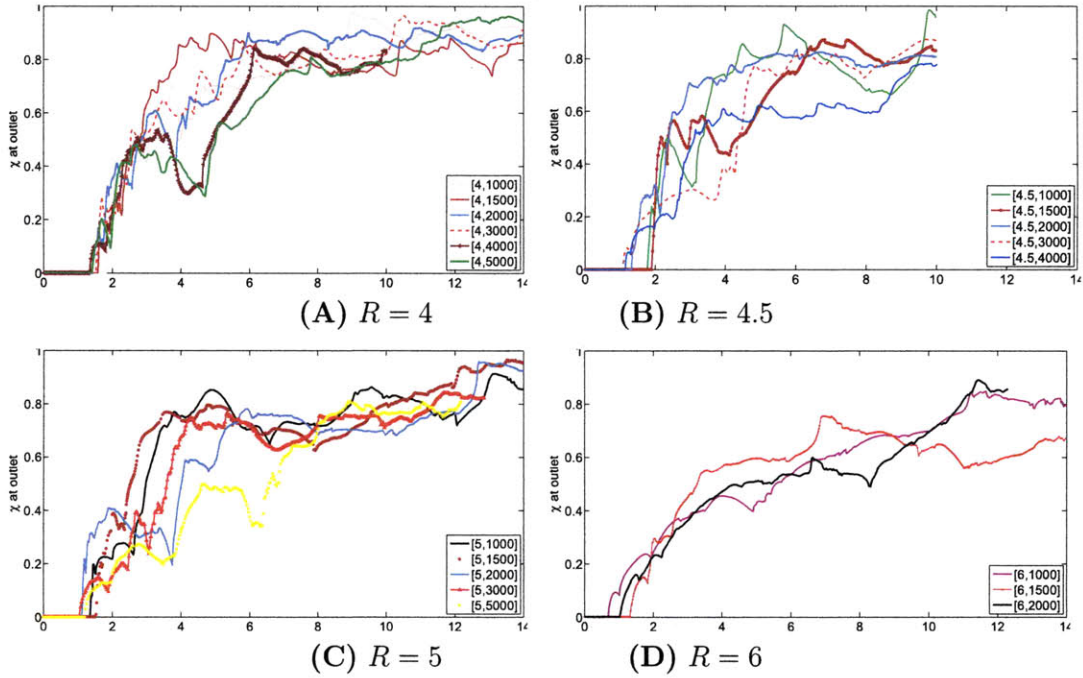
Figure 4-3: Degree of mixing at the outlet plotted for four different R. Each figure shows the effect due to variation in Pe. Comparing these figures to bottom two figures in Fig. 4-2, we see that χ is more sensitive to Pe at higher R. At high R, as channeling starts to dominate the flow, mixing becomes more sensitive to Pe. Higher Pe results in severe tip-splitting, splitting on the sides and branching of the fingers. It takes longer to achieve pseudo-steady state in χ, especially since it is measured at the outlet.

a desired degree of mixing. We note that, for highly diffusive system i.e. low Pe, vigorous fingering at high R is desirable because it spreads the less viscous fluids over larger area of the more viscous domain where it is quickly mixed. Also, at higher R fingers can travel faster to connect successive slugs for better overall mixing.

At higher Pe the mixing curve becomes less sensitive to Pe as expected. We obtain an R that gives quickest mixing and this optimum R is higher for lower χ because only few fingers are required to reach such low degree of mixing and they travel faster at high R.

4.1 Scaling for mixing time

Now, we will find a scaling for mixing time in viscous fingering displacements with the existing theory of chaotic mixing. It is well-known that under chaotic advection (e.g. time-periodic Sine Flow) the concentration field decays exponentially in time,

$$c\left(\boldsymbol{x}, t\right) \sim e^{-\lambda t} \tag{4.1}$$

which is equivalent to decay of the L^2 norm of concentration field,

$$\langle c^2 \rangle^{0.5} = |c| \sim e^{-\lambda t} \tag{4.2}$$

This is also true in a purely straining flow which stretches the material interface in one direction and contracts in orthogonal direction [47]. In that simple case, λ is the rate of strain, $\partial u_x / \partial x = -\partial u_y / \partial y$. In general, λ depends on the mixing protocol and has been related to the dominant eigenvalue of the advection-diffusion operator [7]. In chaotic mixing, λ is a function of R and Pe and it can vary in time and space.

In Fig. 4-5 we demonstrate that $\langle |\boldsymbol{g}| \rangle$ can be taken as a surrogate for interface length. To investigate the influence of R on $\langle |\boldsymbol{g}| \rangle$, we plot interface length at different R in Fig. 4-7. Notice the non-monotonic behaviour of interface length with R. As R increases from 0, it sharply increases, then it stays more or less constant for R
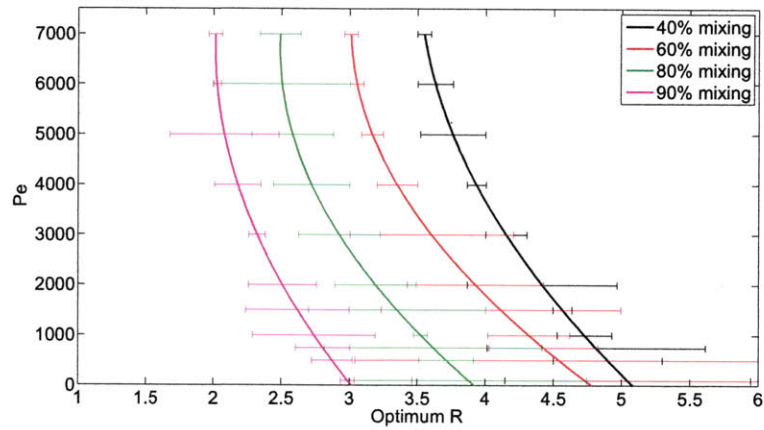
Figure 4-4: For each χ, a mixing curve can be obtained which shows optimum R at each Pe. Uncertainty in determining optimum R is also shown through error bars. This uncertainty is usually higher at low Pe when the effect of initial random perturbations at the front is more prominent. For higher degree of mixing, optimum R is lower. With respect to Pe, optimum R is higher at lower Pe because this combination creates thick fingers which mix quickly in the transverse direction as diffusivity is high.
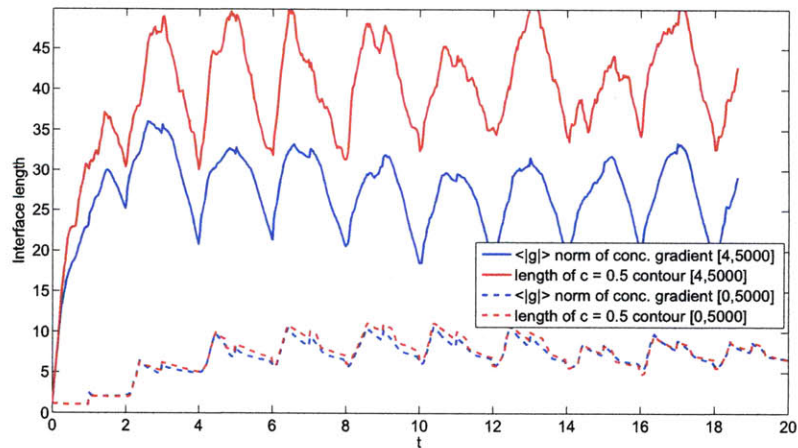
Figure 4-5: Norm of concentration gradient, i.e., $\langle|\boldsymbol{g}|\rangle V$ compares well with the length of $c = 0.5$ contour. This demonstrates the validity of interpreting norm of concentration gradient as similar to the length of the interface between the fluids. Oscillations result from alternating-injection boundary.
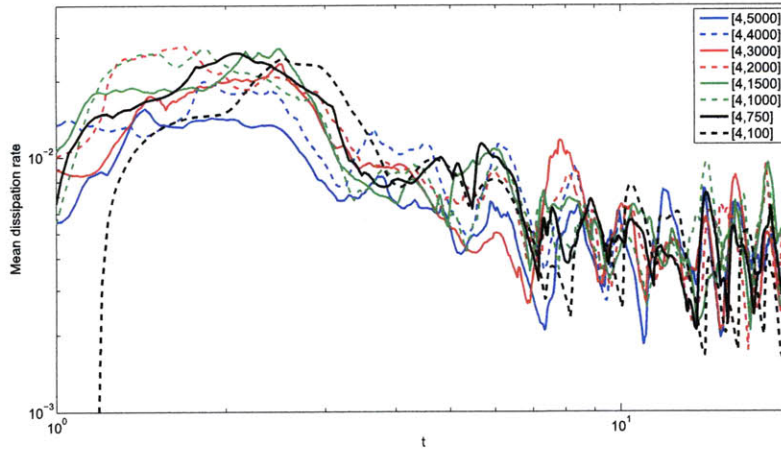
Figure 4-6: Mean dissipation rate is maximum in optimum Pe range of 1000-2000 at $R = 4$. In the diffusive regime, that is after the hump, ϵ is almost independent of Pe.

between 2 and 3 and then it starts to decrease again with sharper drop at $R = 5$ and 6.

We know that in chaotic advection (e.g. prototypical straining flow which resembles viscous fingering) mixing time is related to λ as follows,

$$\lambda t \simeq \log Pe^{1/2} \tag{4.3}$$

Asymptotically, λ scales with Pe as $Pe^{-\zeta}$ where ζ is,

$$\zeta = \begin{cases} 1 & \text{pure diffusion} \\ 0.5 & \text{two-dimensional autonomous flows} \\ 0 & \text{two-dimensional globally chaotic flows} \end{cases} \tag{4.4}$$

Two-dimensional autonomous flows with a velocity field nonlinearly varying in space but fixed in time are not globally chaotic and islands of regular mixing persist in the background of chaotic mixing. The scaling observed with respect to Pe is claimed to be a result of convection-enhanced diffusivity along the contracting direction of flow along which huge gradients are created thereby increasing the efficiency of diffusion. Convection-enhanced diffusion has been reported in the literature through boundary-

77

Figure 4-7: Interface length computed from norm of the concentration field are plotted for different R at $Pe = 5000$, except for $R = 6$ for which $Pe = 2000$. Notice that at any given time, interface length increases as R increases from 0 to 4 and then the interface length decreases for higher R. Thus, interface length behaves non-monotonically with R and is maximum at the optimum R which is between 2 and 3 for alternating-injection setup.
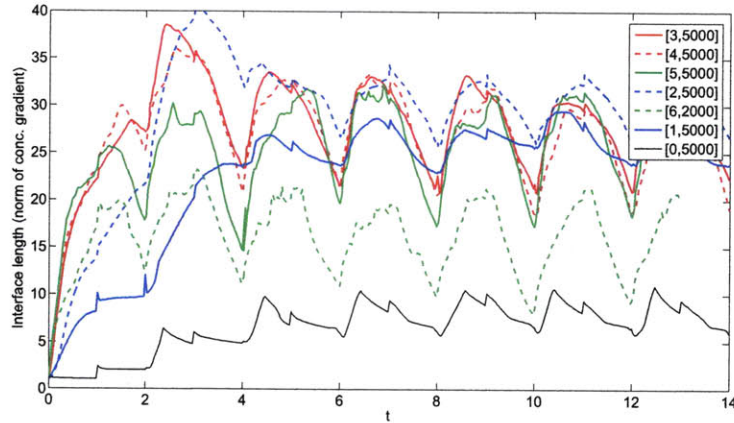
layer analysis [9], Lagrangian simulations [38] and variational methods [11]. Viscous fingering displacements have similarity to such autonomous flows as fingers stretch along a preferential direction and contract along the orthogonal direction.

Fig. 4-8 plots mixing time as a function of R. Notice the non-monotonic behaviour of mixing time with R. Comparing this plot to Fig. 1-2, we clearly see that our starting hypothesis of achieving chaotic mixing conditions by increasing viscosity contrast was incorrect. Viscous fingering does not lead to chaotic mixing conditions at high R. In fact, at very high mobility ratios mixing time starts to increase because of the strong channeling effect which is a result of nonlocal coupling between pressure field and the concentration field created through the mobility Eq .(1.4).

In Fig. 4-8, mixing time for $R = 1$ is from a single-slug simulation in a periodic domain as degree of mixing can not reach 0.8 for $R \leq 1$ in alternating-injection simulations, with the slug ratio (less viscous to more visocus) and slug pore volume (ratio of slug volume to domain volume) used in these simulations. This curve successfully captures the sharp drop in mixing time as R increases above 1, then stays more or less flat and again starts to rise from $R > 4$.

78
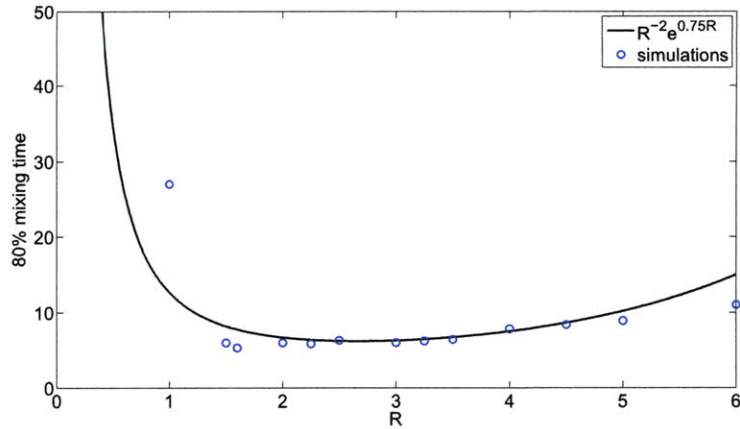
Figure 4-8: Mixing time changes non-monotonically with R. There is an optimum R corresponding to minimum mixing time, which depends on Pe. Above, $Pe = 5000$ except for $R = 6$, for which $Pe = 2000$.

Fig. 4-9 plots minimum mixing time as a function of Pe to allow comparison with the scaling in globally chaotic mixing $t_{\text{chaotic}} \sim \log Pe^{1/2}$, 2D autonomous flows $t_{\text{auto}} \sim Pe^{1/2}$, and purely diffusive mixing $t_{\text{diff}} \sim Pe$. Note that the similarity between viscous fingering and autonomous flows will not be achieved for $R = 0$ but for an R that results in a velocity field closest to chaotic advection which means optimum R for that Pe.

As the desired degree of mixing increases, the scaling tilts in favor of diffusive mixing protocol which is expected because it takes more time to mix the fluids to a higher degree of mixing.
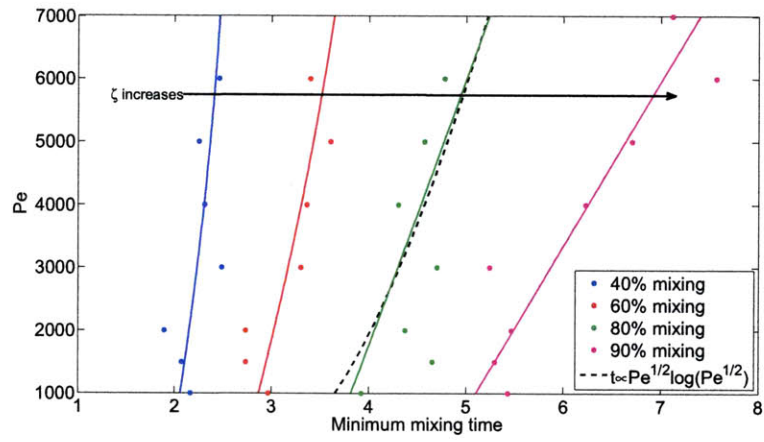
Figure 4-9: Minimum mixing time in viscous fingering displacements increases with Pe as Pe^ζ, with exponent depending on the desired degree of mixing.

Chapter 5

Anisotropy and inhomogeneity of mixing

Mixing becomes inhomogeneous because concentration and velocity fields are not uniformly distributed over the domain. In chaotic mixing, inhomogeneity is visualized as islands bounded with large concentration gradients scattered around in a background chaotic flow where islands denote regions of regular mixing (particles diverging linearly in time, as opposed to exponentially). Effective diffusion coefficient changes in space with concentration. In fact, it is possible to compute 'effective diffusivity' for each concentration, using area of the contour as a Lagrangian coordinate [26], as derived in Appendix A.2.

Inhomogeneity in mixing can be understood as inhomogeneity in effective diffusivity as defined in Eq. (2.62). Fig. 5-1 plots this effective diffusivity, normalized to molecular diffusivity i.e. $D_{\text{eff}}/D = L_e^2/L_y^2$, as a function of time and concentration. Fig. 5-2 plots normalized effective diffusivity as a function of time and equivalent length. Equivalent length is computed by dividing the area enclosed within certain contour by the minimum geometric height possible for a typical contour which in our case is $L_y = W$, i.e., width of the domain. Area enclosed by a contour is defined in Eq. (A.5), hence, it increases with value of the contour because it is cumulative. Therefore, the range of values on y axis in both Fig. 5-1 and Fig. 5-2 are equivalent.

Fig. 5-2 can be interpreted as follows. Initially, when there is a slug of less viscous
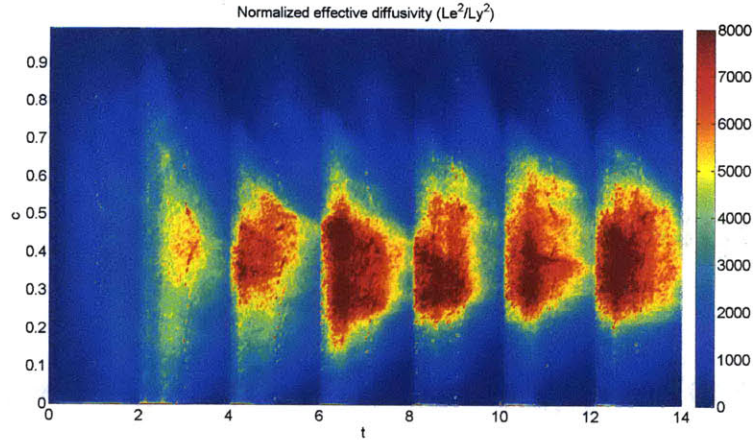
Figure 5-1: Normalized effective diffusivity during alternating injection viscous fingering displacement for [4,5000].

fluid in a more visocus medium with a flat front, most of the mass is enclosed by the contour of $c = 0$ and the range in equivalent length is very small. Later, this range expands as viscous fingers stretch and deform the contours, distributing mass among all the contours. We also see the oscillatory behaviour due to alternating injection. But most importantly we see that color-coded diffusivity is not same for all the concentration contours. It is highest for a range of concentrations around $c = 0.5$. A lower effective diffusivity for $c = 1$ contour may explain the sharpness of finger tip, or suppression of Taylor dispersion which occurs because tip velocity is higher than mean flow velocity. In general, spatially varying effective diffusivity allowes edges in concentration field. We also notice that effective diffusivity quickly increases with time to a pseudo-steady state value which is smaller for higher R (Fig. 5-3).

Effective diffusivity is also influenced by Pe. At optimum R of 2.5 (for $\chi = 0.8$) in alternating-injection simulations, it increases for $Pe = 10000$ as shown in Fig. 5-5 and we can see that in degree of mixing curve in Fig. 5-6 as well.

Anisotropy in chaotic mixing and turbulent mixing has also its counterpart in viscous fingering displacements. Longitudinal direction corresponds to unstable direction along which interface lines stretch. Interesting things happen along transverse direction. There is a competition between shrinking process along this kinematically
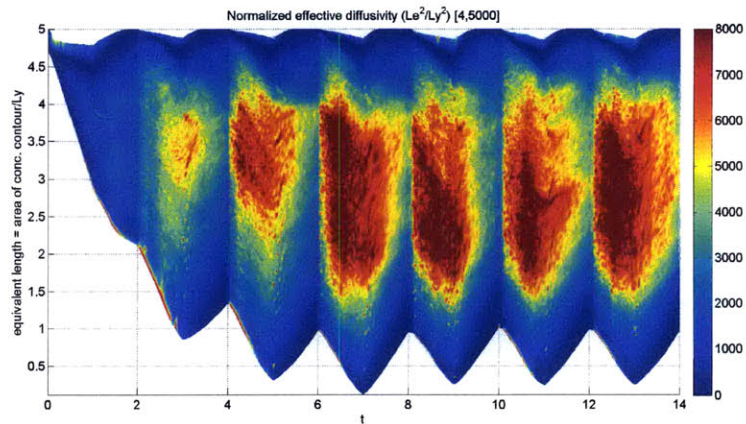
Figure 5-2: .
]Normalized effective diffusivity against equivalent length for [4,5000]. The sawtooth profile is due to alternating-injection boundary. Notice that effective diffusivity is maximum around $c = 0.5$. Also, for the duration of the plot, it increase with time. At very late times (not shown above), effective diffusivity goes to zero as seen in Fig. 2-15 and Fig. 2-16
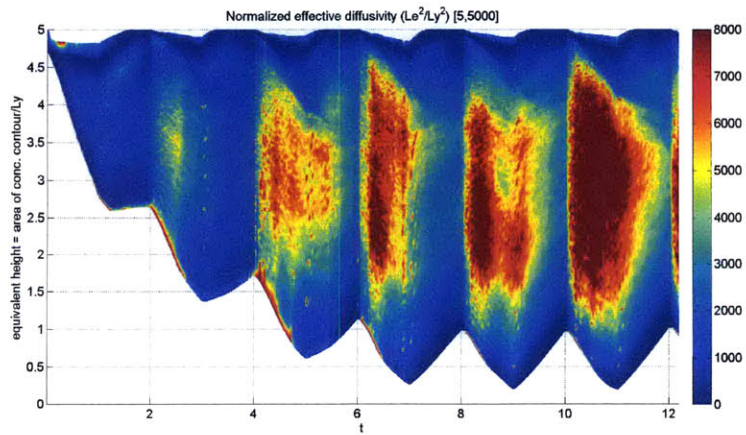
Figure 5-3: Normalized effective diffusivity is smaller for $R = 5$ which corresponds to reduced mixing.
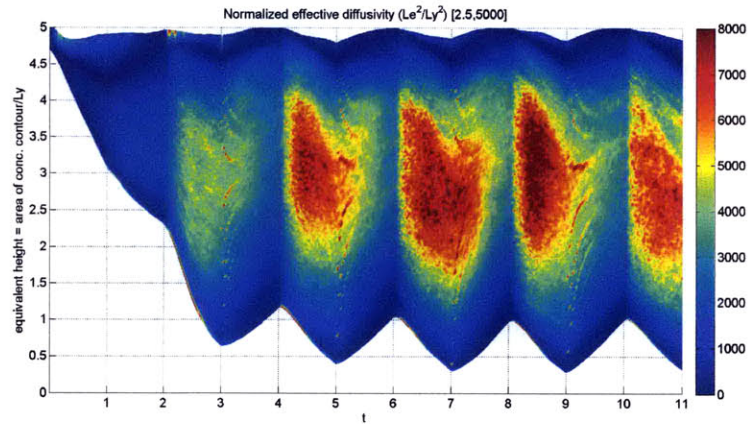
Figure 5-4: Lower normalized effective diffusivity at relatively low Pe.
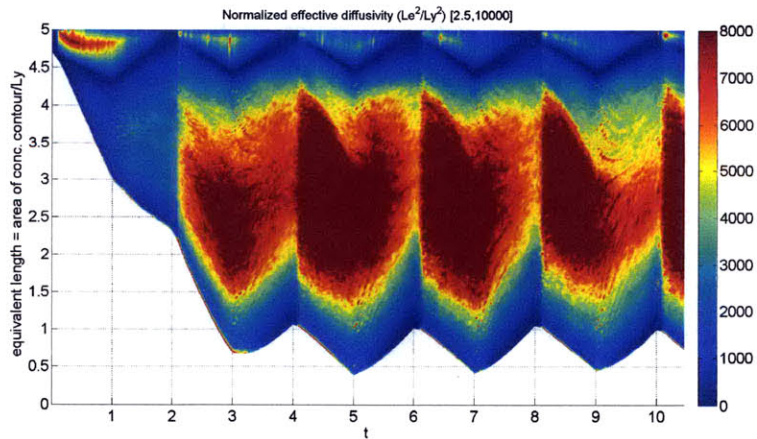
Figure 5-5: Higher normalized effective diffusivity at higher Pe.
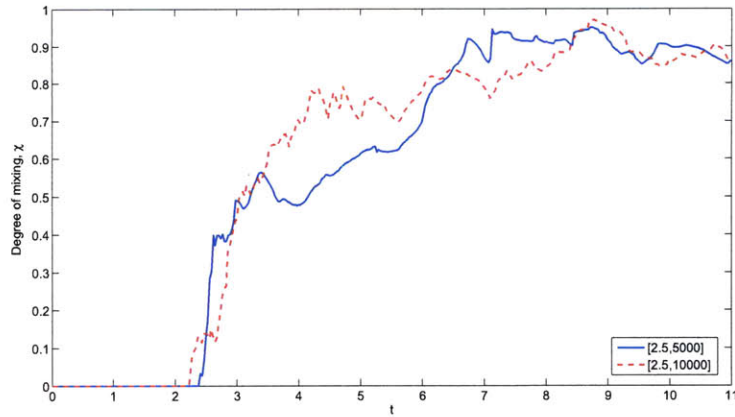
Figure 5-6: Degree of mixing at outlet reflects the effect of low effective diffusivity in case of $Pe = 5000$.
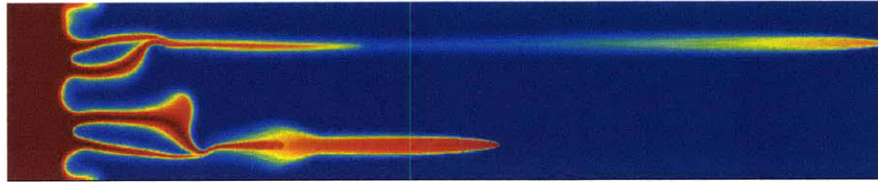
Figure 5-7: Pinch off at high R and low Pe. Diffusion wipes out the steep gradient created by fast moving finger. [6,1000].

stable direction and diffusional growth. Ratio of the time scales of these two processes play an important role in determining the structure of the finger as it grows. Moreover, at high R when tip velocity is very high, the transverse thickness can shrink a lot in short time creating very high gradients that diffusion will remove by pinching off the finger neck (Fig. 5-7). Longitudinal dispersion and transverse dispersion are different which has consequences in terms of growth rate and preferred length scale of the instability [43]. Defining anisotropy in dispersion, β, as ratio of transverse dispersion coefficient to longitudinal dispersion coefficient, D_T/D_L, and assuming empirical relations between dispersion coefficient and velocity, Tan and Homsy came up with relations that modify Eq. (2.1) such that growth rate increases almost ten times when $\beta \to 0$ and decreases by a factor of $O(\beta^{-1})$ when $\beta \to \infty$. Respectively, finger length scale decreases by a factor of $O(\beta^{1/3})$ and increase by a factor of $O(\beta)$.
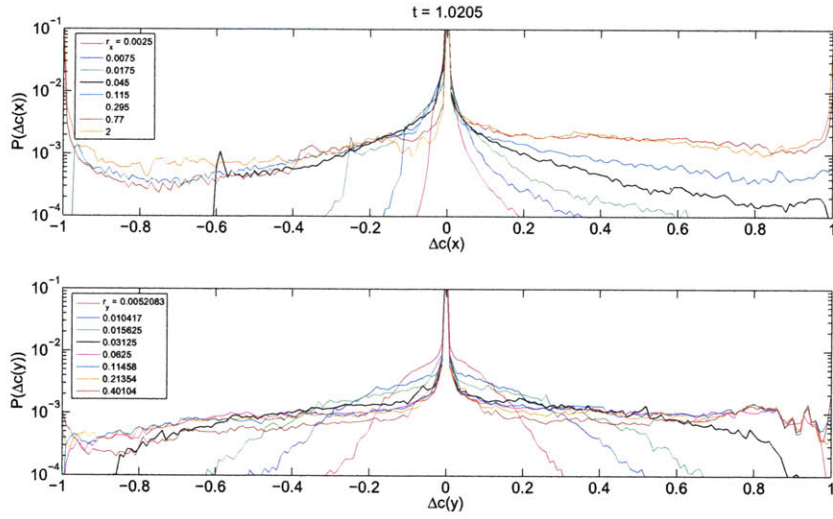
Figure 5-8: Histogram of Δc along x and y directions for various separation distances r. Single-slug simulation at $R = 3$, $Pe = 5000$. Notice higher symmetry along y than along x because of a mean gradient in x.

Anisotropy can also be observed in the evolution of concentration field statistics along and across the flow directions. Histograms of concentration differences at specific distances are shown in Fig. 5-8. These histograms are symmetric in y and not in x which is expected because of a mean gradient imposed in x. As the separation increases, the histogram evolves from stretched exponential to Gaussian. Kurtosis also behaves differently as a function of separation (Fig. 5-9). The return to Gaussian isotropy (i.e. Kurtosis $= 3$) is faster and starts at much higher Kurtosis in x direction than in y.
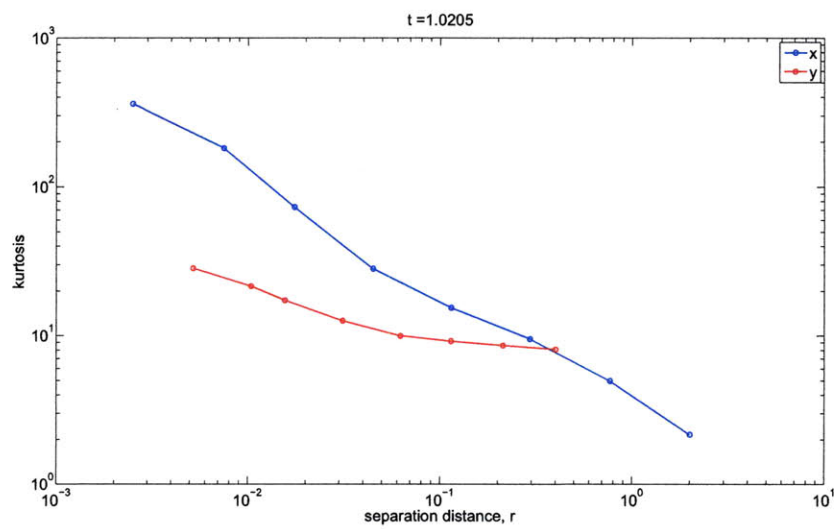
Figure 5-9: Kurtosis of Δc along x and y directions for various separation distances r. Single-slug simulation at $R = 3$, $Pe = 5000$. Notice that kurtosis for nearby points is higher along x because of a mean gradient in x.

Chapter 6

Conclusions

Mixing in viscous fingering displacements is a result of nonlinear coupling of velocity and concentration fields, is neither homogeneous nor isotropic and is not as efficient as chaotic mixing. It is also not similar to the traditional turbulent mixing because of the same coupling. However, it is possible to derive optimum mixing conditions following a volume-averaged approach that captures the characteristic stretching of the material interface over which diffusive mixing takes place. Optimality of the governing parameters, the mobility ratio and the Peclet number, results from the non-monotonic dependence of total interface length on these parameters. Therefore, mixing time becomes a non-monotonic function of these two parameters, with weaker dependence on Peclet number at higher Peclet number. We also conclude that optimum mobility ratio weakly depends on Peclet number.

Two important extensions to the proposed two-equation model will be:

1. Non-periodic boundary conditions - We have derived the two-equation model under periodic boundary conditions which enforces constant mean concentration and a purely decaying variance. Periodicity allows us to make other assumptions as well. It will be useful to extend the model with a forcing term that reflects $\langle c \rangle = \langle c \rangle(t)$, i.e., a time-varying mean concentration. This will lead to (at least) a production/destruction term in the variance equation, driven by the boundary conditions.

2. Mechanical energy dissipation - It should be possible to extend the model to capture the decay of mean kinetic energy and the evolution of mean energy dissipation rate, analogous to the two-equation model. This can be done under Darcy flow assumption which is suitable for the porous media flows. Mechanical dissipation model can give us a velocity scale during the mixing process and allow us to define a 'fingering diffusivity' with the help of mean scalar dissipation rate. This will provide further insight into the mixing process.

The extended two-equation model should eventually lead us to create a subgrid model of viscous fingering. One should be able to perform 'under-resolved' simulations with an effective diffusivity at each gridblock that combines the effect of molecular and convective mixing. This dynamic 'fingering diffusivity' should go to zero as the grid is refined.

Appendix A

Appendix

A.1 The $k - \epsilon_u$ model in turbulence

These equations express the transport of kinetic energy and dissipation rate in the domain due to turbulence exchange and homogenization processes.

$$\frac{\partial k}{\partial t} + \boldsymbol{U}\nabla k - \frac{c_\mu}{2}\frac{k^2}{\epsilon_u}\left|\nabla \boldsymbol{U} +^t \nabla \boldsymbol{U}\right|^2 - \nabla \cdot \left(c_\mu \frac{k^2}{\epsilon_u}\nabla k\right) + \epsilon_u = 0, \qquad \text{(A.1)}$$

$$\frac{\partial \epsilon_u}{\partial t} + \boldsymbol{U}\nabla \epsilon_u - \frac{c_1}{2}k\left|\nabla \boldsymbol{U} +^t \nabla \boldsymbol{U}\right|^2 - \nabla \cdot \left(c_\epsilon \frac{k^2}{\epsilon_u}\nabla \epsilon_u\right) + c_2\frac{\epsilon_u^2}{k} = 0 \qquad \text{(A.2)}$$

where $c_\mu = 0.09$, $c_1 = 0.126$, $c_2 = 1.92$, and $c_\epsilon = 0.07$ are presumably universal constants. $\boldsymbol{U}$ is the mean velocity field which is obtained by solving the Navier-Stokes equation written for $\boldsymbol{U}$, also known as Reynolds equation:

$$\frac{\partial \boldsymbol{U}}{\partial t} + \boldsymbol{U}\nabla \boldsymbol{U} + \nabla\left(P + \frac{2}{3}k\right) - \nabla \cdot \left[(\nu + \nu_T)\left(\nabla \boldsymbol{U} +^t \nabla \boldsymbol{U}\right)\right] = 0, \quad \nabla \cdot \boldsymbol{U} = 0,$$

$$\text{(A.3)}$$

where P is the mean pressure field. Kinetic energy and mechanical dissipation rate are defined as,

$$k = \frac{1}{2}\langle|\boldsymbol{u}'|^2\rangle, \qquad\qquad \epsilon_u = \frac{\nu}{2}\langle|\nabla\boldsymbol{u}' +^t \nabla\boldsymbol{u}'|^2\rangle, \qquad (A.4)$$

where $\boldsymbol{u} = \boldsymbol{U} + \boldsymbol{u}'$ is the total velocity field. The $k - \epsilon_u$ model is derived heuristically from the Navier-Stokes equations with following hypotheses:

1. Reynolds hypothesis for $\langle\boldsymbol{u}' \otimes \boldsymbol{u}'\rangle$ and $\langle\boldsymbol{\omega}' \otimes \boldsymbol{\omega}'\rangle$ which says both these tensors are functions of $\nabla\boldsymbol{U} +^t \nabla\boldsymbol{U}$, k, and ϵ_u only. Here, $\boldsymbol{\omega}' = \nabla \times \boldsymbol{u}'$. The coefficient of proportionality between $\langle\boldsymbol{u}' \otimes \boldsymbol{u}'\rangle$ and $\nabla\boldsymbol{U} +^t \nabla\boldsymbol{U}$ is effective viscosity ν_T. Effective viscosity ν_T is a polynomial function of k and ϵ_u, more explicitly, $\nu_T = c_\mu k^2/\epsilon_u$.

2. $|\boldsymbol{u}'|^2$ and $|\nabla \times \boldsymbol{u}'|^2$ are passive scalars when advected by $\boldsymbol{u}$. Convection by random fields produces diffusion for the mean.

3. Ergodicity allows statistical averages to be space averages.

4. Local homogeneity of the turbulence. Isotropy of $\boldsymbol{u}'$ to neglect all odd boundary integrals after integration by parts.

5. Quasi-Gaussian turbulence so as to neglect $\langle\boldsymbol{\omega}' \otimes \boldsymbol{\omega}' : \nabla\boldsymbol{u}'\rangle$.

6. A closure hypothesis to model $\nu^2\langle|\nabla \times \boldsymbol{\omega}'|^2\rangle$ or $\nu^2\langle|\nabla\boldsymbol{\omega}'|^2\rangle$ as $c_2\epsilon_u^2/k$.

We will compare the $k - \epsilon_u$ model for mechanical dissipation to the proposed $\sigma^2 - \epsilon$ model for passive scalar mixing. Notice that c_μ terms are zero in case of σ^2 evolution equation, precisely because of the periodicity assumption (constant mean and zero contribution from boundary integrals). First two terms on LHS of k equation is equivalent to the total time derivative of variance in our two-equation model. Similarly, in the comparison between ϵ_u equation and ϵ equation, the divergence term with c_ϵ in ϵ_u equation is zero in case of ϵ equation because of the imposed periodicity. Fifth term in Eq. (A.2), $c_2\frac{\epsilon_u^2}{k}$, is the rate of homogenization of the dissipation rate and it is similar to $B\frac{\epsilon^2}{\sigma^2}$ term in Eq. (2.49) which also plays the same role for scalar.

92

The only term remaining in the ϵ equation without an obvious counterpart in ϵ_u equation is the $\epsilon^{3/2}$ term which is responsible for an increase in ϵ. Basically, in the derivation of ϵ_u model equation, $\langle \boldsymbol{\omega}' \otimes \boldsymbol{\omega}' \rangle$ term is taken as equal to $a\boldsymbol{I} - c_1 k \left(\nabla \boldsymbol{U} +^t \nabla \boldsymbol{U} \right)$ where $\boldsymbol{I}$ is the Identity matrix and a is a constant. Therefore, $\langle \nabla \boldsymbol{U} : \boldsymbol{\omega}' \otimes \boldsymbol{\omega}' \rangle$ gives the third term in Eq. (A.2). In our two-equation model, we express $\langle |\boldsymbol{g} \otimes \boldsymbol{g}| \rangle$ as $Pe\epsilon$ which multiplies $\langle |\nabla^s \boldsymbol{u}| \rangle$ to produce $-RU(Pe\epsilon)^{3/2}$. Hence, the analogy between these two models continues for this term as well.

A.2 Derivation of effective diffusivity

We follow derivation of effective diffusivity through Lagrangian-mean method as described in [26]. It is called Lagrangian-mean method because mean of any scalar quantity over a contour is defined with respect to the area enclosed by that contour which is equivalent to the mass enclosed by that contour and mass can be used as a Lagrangian coordinate. The other aspect of this derivation is that the enclosed area can be defined such that it is always a monotonically increasing function of concentration and, therefore, area coordinate can be replaced by concentration coordinate. In short, tracer itself becomes a coordinate along which mass trasport is analyzed. Using tracer as a coordinate has two advantages: (i) the geometrical complexity and the location of the transport barrier are absorbed in the coordinate so they do not hinder analysis, and (ii) instantaneous, irreversible transport can be extracted. The tracer isosurface is a material surface in the absence of diffusion, so the mass transport in the tracer coordinate arises solely from diffusion (therefore it is irreversible by definition). Yet its magnitude depends on the geometry of tracer and hence affected by the flow: where stirring is strong, the tracer geometry becomes complex and mass exchange is enhanced. The area (mass) the fluid occupies in regions where $c \leq c^*$ at a given time t, where c^* is a chosen value of c, is also the area enclosed by contour $c = c^*$ and it is defined as,

$$A(c^*, t) \equiv \int_{c \leq c^*} \mathrm{d}S, \tag{A.5}$$

93

The change in this area from time t to $t + \delta t$ is

$$\delta \int_{c \leq c^*} \mathrm{d}S = \int_{c(t+\delta t) \leq c^*} \mathrm{d}S - \int_{c(t) \leq c^*} \mathrm{d}S \qquad (A.6)$$

Using the identity,

$$\oint_{c=c^*} \frac{(\,\cdot\,)}{|\nabla c|} \mathrm{d}l = \frac{\partial}{\partial c^*} \int_{c \leq c^*} (\,\cdot\,) \, \mathrm{d}S, \qquad (A.7)$$

we have,

$$\delta \int_{c \leq c^*} \mathrm{d}S \approx - \oint_{c=c^*} \delta t \frac{\partial c/\partial t}{|\nabla c|} \mathrm{d}l = -\delta t \frac{\partial}{\partial c^*} \int_{c \leq c^*} \frac{\partial c}{\partial t} \mathrm{d}S. \qquad (A.8)$$

Dividing by δt, taking limit $\delta t \to 0$ and substituting Eq. (1.1),

$$\frac{\partial}{\partial t} A(c^*, t) = -\frac{\partial}{\partial c^*} \int_{c \leq c^*} \left(\frac{1}{Pe} \nabla^2 c - \nabla \cdot (\boldsymbol{u} c) \right) \mathrm{d}S \qquad (A.9)$$

However, using the divergence theorem,

$$\int_{c \leq c^*} \nabla \cdot (\boldsymbol{u} c) \, \mathrm{d}S = c^* \oint_{c=c^*} \frac{\boldsymbol{u} \cdot \nabla c}{|\nabla c|} \mathrm{d}l = c \int_{c \leq c^*} \nabla \cdot \boldsymbol{u} \mathrm{d}S = 0 \qquad (A.10)$$

Hence,

$$\frac{\partial}{\partial t} A(c^*, t) = -\frac{1}{Pe} \frac{\partial}{\partial c^*} \int_{c \leq c^*} \nabla^2 c \mathrm{d}S, \qquad (A.11)$$

which can be further transformed using Eq. (A.7) into,

$$\frac{\partial}{\partial t} A(c^*, t) = -\frac{1}{Pe} \frac{\partial}{\partial c^*} \left(\langle |\nabla c|^2 \rangle_{c^*} \frac{\partial A}{\partial c^*} \right), \qquad (A.12)$$

where the subscripted angular bracket denotes the average of a field variable on the tracer contour $c = c^*$, defined as

$$\langle \,\cdot\, \rangle_{c^*} \equiv \frac{\partial}{\partial A} \int_{c \leq c^*} (\,\cdot\,) \, \mathrm{d}S \qquad (A.13)$$

Eq. (A.12) can be expressed in terms of mean dissipation rate as,

$$\frac{\partial A}{\partial t} = -\frac{\partial}{\partial c^*} \left(\epsilon^* \frac{\partial A}{\partial c^*} \right), \qquad (A.14)$$

94

where ϵ^* is the dissipation rate of tracer variance for $c = c^*$, also known as conditional dissipation rate.

Since area-concentration relationship is one-to-one, A can be substituted by c^* in Eq. (A.12) as follows,

$$\frac{\partial}{\partial t} c^* (A, t) = -\frac{\partial c^*}{\partial A} \frac{\partial A}{\partial t} = \frac{1}{Pe} \frac{\partial}{\partial A} \left(\langle |\nabla c|^2 \rangle_{c^*} \frac{\partial A}{\partial c^*} \right). \tag{A.15}$$

The minus sign in the second expression is because an increase in A at a fixed c^* causes a decrease in c^* at a fixed A when A is an increasing function of c^*. Hence we can write,

$$\frac{\partial}{\partial t} c^* (A, t) = \frac{1}{Pe} \frac{\partial}{\partial A} \left(L_e^2 \frac{\partial c^*}{\partial A} \right), \tag{A.16}$$

where *effective length*, L_e is defined as,

$$L_e^2(A, t) \equiv \frac{\langle |\nabla c|^2 \rangle_{c^*}}{(\partial c^* / \partial A)^2}. \tag{A.17}$$

In deriving Eq. (A.16), advective transport is absorbed in the motion of the area coordinate and therefore irreversible mixing effects are isolated from the effects of advection.

Bibliography

[1] J. C. Bacri, N. Rakotomalala, D. Salin, and R. Woumeni. Miscible viscous fingering: Experiments versus continuum approach. *Phys. Fluids*, 4:1611, 1992.

[2] G. I. Barenblatt. *Scaling, self-similarity, and intermediate asymptotics*. Camb. Univ. Press, 1996.

[3] J. Bear. *Dynamics of Fluids in Porous Media*. Wiley, 1972.

[4] G. Boffetta, F. De Lillo, and S. Musacchio. Nonlinear diffusion model for Rayleigh-Taylor mixing. *Phys. Rev. Lett.*, 104:034505, 2010.

[5] G. Boffetta, A. Mazzino, S. Musacchio, and L. Vozella. Polymer heat transport enhancement in thermal convection: The case of Rayleigh-Taylor turbulence. *Phys. Rev. Lett.*, 104:184501, 2010.

[6] E. Buckingham. On physically similar systems; Illustrations of the use of dimensional equations. *Phys. Rev.*, 4:345, 1914.

[7] S. Cerbelli, A. Adrover, F. Creta, and M. Giona. Foundations of laminar chaotic mixing and spectral theory of linear operators. *Chem. Eng. Sci.*, 61:2754, 2006.

[8] C.-Y. Chen and E. Meiburg. Miscible displacements in a capillary tube. Part 2. Numerical simulations. *J. Fluid Mech.*, 326:57, 1996.

[9] S. Childress and A. M. Soward. Scalar transport and alpha-effect for a family of cats-eye flows. *J. Fluid Mech.*, 205:99, 1989.

[10] V. Eswaran and S. B. Pope. Direct numerical simulations of the turbulent mixing of a passive scalar. *Phys. Fluids*, 31:506, 1988.

[11] A. Fannjiang and G. Papanicolau. Convection enhanced diffusion for periodic flows. *J. Appl. Maths*, 54:333, 1994.

[12] D. R. Fereday, P. H. Haynes, and A. Wonhas. Scalar variance decay in chaotic advection and Batchelor-regime turbulence. *Phys. Rev. E*, 65:035301, 2002.

[13] J. W. Gardner and J. G. J. Ypma. An investigation of phase behavior macroscopic bypassing interaction in CO_2 flooding, SPE 10686.

[14] N. Goyal and E. Meiburg. Miscible displacements in Hele-Shaw cells: Two-dimensional base states and their linear stability. *J. Fluid Mech.*, 558:329, 2006.

[15] J. O. Hinze. *Turbulence, An introduction to its mechanism and theory*. McGraw Hill, 1959.

[16] G. M. Homsy. Viscous fingering in porous media. *Ann. Rev. Fluid Mech.*, 19:271, 1987.

[17] M.-C. Jullien, P. Castiglione, and P. Tabeling. Experimental observation of Batchelor dispersion of passive tracers. *Phys. Rev. Lett.*, 85:3636, 2000.

[18] B. E. Launder and D. B. Spalding. *Mathematical models of Turbulence*. Academic Press, 1972.

[19] D. Loggia, N. Rakotomalala, D. Salin, and Y. C. Yortsos. Evidence of new instability thresholds in miscible displacements in porous media. *Europhys. Lett.*, 32:633, 1995.

[20] J. M. MacInnes, Z. Chen, and R. W. K. Allen. Investigation of alternating-flow mixing in microchannels. *Chem. Eng. Sci.*, 60:3453, 2005.

[21] A. J. Majda and P. R. Kramer. Simplified models for turbulent diffusion: Theory, numerical modelling, and physical phenomena. *Phys. Reports*, 314:237, 1999.

[22] O. Manickam and G. M. Homsy. Fingering instabilities in vertical miscible displacement flows in porous media. *J. Fluid Mech.*, 288:75, 1995.

[23] D. W. McLaughlin, G. C. Papanicolaou, and O. R. Pironneau. Convection of microstructure and related problems. *SIAM J. Appl. Math.*, 45:780, 1985.

[24] M. Muradoglu and H. Stone. Mixing in a drop moving through a serpentine channel: A computational study. *Phys. Fluids*, 17:073305, 2005.

[25] S. Nagata. *Mixing : principles and applications*. Wiley, 1975.

[26] N. Nakamura. Two-dimensional mixing, edge formation, and permeability diagnosed in an area coordinate. *J. Atmos. Sci.*, 53:1524, 1996.

[27] J. Ottino. *The Kinematics of Mixing: Stretching, Chaos, and Transport*. Camb. Univ. Press, 1989.

[28] J. Ottino. The mixing of fluids. *Sci. Am.*, 260:56, 1989.

[29] J. Ottino. Mixing, chaotic advection, and turbulence. *Ann. Rev. Fluid Mech.*, 22:207, 1990.

[30] M. Overholt and S. B. Pope. Direct numerical simulation of a passive scalar with imposed mean gradient in isotropic turbulence. *Phys. Fluids*, 8:3128, 1996.

[31] L. Paterson. Fingering with miscible fluids in a Hele-Shaw cell. *Phys. Fluids*, 28:26, 1985.

[32] R. L. Perrine. A unified theory for stable and unstable miscible displacement. *Soc. Pet. Eng. J.*, 228:205, 1963.

[33] P. Petitjeans and C.-Y. Chen. Miscible quarter five-spot displacements in a Hele-Shaw cell and the role of flow-induced dispersion. *Phys. Fluids*, 11:1705, 1999.

[34] P. Petitjeans and T. Maxworthy. Miscible displacements in capillary tubes. Part 1. Experiments. *J. Fluid Mech.*, 326:37, 1996.

[35] D. Pritchard. The instability of thermal and fluid fronts during radial injection in a porous medium. *J. Fluid Mech.*, 508:133, 2004.

[36] A. Pumir. A numerical study of the mixing of a passive scalar in three dimensions in the presence of a mean gradient. *Phys. Fluids*, 6:2118, 1994.

[37] A. Riaz, C. Pankiewitz, and E. Meiburg. Linear stability of radial displacements in porous media: Influence of velocity-induced dispersion and concentration-dependent diffusion. *Phys. Fluids*, 16:3592, 2004.

[38] M. N. Rosenbluth, H. L. Berk, I. Doxas, and W. Horton. Effective diffusion in laminar convective flows. *Phys. Fluids*, 30:2636, 1987.

[39] P. A. Rottenburg. Mixing–theory related to practice. In AIChE, editor, *Symposium on Mixing–Theory Related to Practice*, London, 1965. Institution of Chemical Engineers.

[40] H. Salman and P. H. Haynes. A numerical study of passive scalar evolution in peripheral regions. *Phys. Fluids*, 19:067101, 2007.

[41] W. R. Schowalter. Stability criteria for miscible displacement of fluid from a porous medium. *A.I.Ch.E.J.*, page 99, 1965.

[42] A. Stroock, K. Dertinger, and A. Ajdari. Chaotic mixer for microchannels. *Science*, 295:647, 2002.

[43] C. T. Tan and G. M. Homsy. Stability of miscible displacements in porous media: Rectilinear flow. *Phys. Fluids*, 29:3549, 1986.

[44] C. T. Tan and G. M. Homsy. Simulation of nonlinear viscous fingering in miscible displacement. *Phys. Fluids*, 31:1330, 1988.

[45] G. I. Taylor. Dispersion of soluble matter in solvent flowing slowly through a tube. *Proc. R. Soc. London*, Ser. A 219:186, 1953.

[46] H. Tennekes and J. L. Lumley. *A First Course in Turbulence*. The MIT Press, 1972.

[47] J.-L. Thiffeault. Scalar decay in chaotic mixing. In J. B. Weiss and A. Provenzale, editors, *Transport and Mixing in Geophysical Flows, Lecture Notes in Physics 744*, Berlin, 2008. Springer.

[48] V. W. Uhl and J. B. Gray. *Mixing : principles and applications.* Academic Press, 1966.

[49] G. Voth, T. Saint, G. Dobler, and J. Gollub. Mixing rates and symmetry breaking in two-dimensional chaotic flow. *Phys. Fluids*, 15:2560, 2003.

[50] Z. Warhaft and J. Lumley. An experimental study of the decay of temperature fluctuations in grid-generated turbulence. *J. Fluid Mech.*, 88:659, 1978.

[51] K. B. Winters and E. A. Dasaro. Diascalar flux and the rate of fluid mixing. *J. Fluid Mech.*, 317:179, 1996.

[52] A. De Wit. Fingering of chemical fronts in porous media. *Phys. Rev. Lett.*, 87:054502, 2001.

[53] A. De Wit and P. De Kepperb et al. Hydrodynamical instability of spatially extended bistable chemical systems. *Chem. Eng. Sci.*, 58:4823, 2003.

[54] A. De Wit and G. M. Homsy. Viscous fingering in periodically heterogeneous porous media. I.Formulation and linear instability. *J. Chem. Phys.*, 107:9609, 1997.

[55] Z. M. Yang, Y. C. Yortsos, and D. Salin. Asymptotic regimes in unstable miscible displacements in random porous media. *Adv. Water Resour.*, 25:885, 2002.

[56] Y. C. Yortsos. Instabilities in displacement processes in porous media. *J. Phys.: Condensed Matter*, 2, 1990.

[57] W. B. Zimmerman and G. M. Homsy. Nonlinear viscous fingering in miscible displacement with anisotropic dispersion. *Phys. Fluids A*, 3:1859, 1991.

[58] W. B. Zimmerman and G. M. Homsy. Viscous fingering in miscible displacements: Unification of effects of viscosity contrast, anisotropic dispersion, and velocity dependence of dispersion on nonlinear finger propagation. *Phys. Fluids A*, 4:2348, 1992.